Deep–Sea Research I 179 (2022) 103664

Contents lists available at ScienceDirect

Deep-Sea Research Part I

journal homepage: www.elsevier.com/locate/dsri

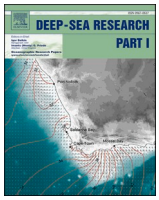

Meanders of the West Greenland Current near Cape Farewell

Astrid Pacini [a,b,*], Robert S. Pickart [b]

[a] MIT-WHOI Joint Program in Physical Oceanography, Woods Hole, MA, USA
[b] Woods Hole Oceanographic Institution; Woods Hole, MA, USA

ARTICLE INFO

Keywords:
Instability processes
Meander formation
Boundary current dynamics
Labrador sea water

ABSTRACT

The cyclonic boundary current that circumnavigates the Labrador Sea plays an important role in modulating the strength of wintertime convection in the interior basin, as well as restratifying the newly ventilated water in spring. Modeling studies indicate that meso and sub-mesoscale processes in the boundary current flux a significant amount of heat and freshwater offshore, although observations of this small-scale variability are lacking. Using four years of data from a mooring array west of Cape Farewell, Greenland, together with satellite altimetry and sea surface temperature measurements, we present the first observations of a meandering West Greenland Current. We describe the statistics, structure, characteristics, and formation mechanism of these features. The meanders occur roughly 30% of the time and are more prevalent in winter and early spring, with an increasing trend over the four-year record. It is shown that baroclinic instability of the boundary current is the cause of the meanders, triggered by seasonal steepening of the isopycnals between the interior basin and the boundary due to offshore convection. We argue that the meandering leads to the formation of small-scale eddies, and estimate the resulting seaward heat flux. Finally, possible connections between the meanders and the production of Irminger Rings are explored.

1. Introduction

Open-ocean convection in the Labrador Sea produces intermediate waters that contribute to the lower limb of the Atlantic Meridional Overturning Circulation (AMOC). The formation and subsequent spreading of these intermediate waters helps to regulate the circulation and stratification of the subpolar North Atlantic (Talley and McCartney, 1982; Sy et al., 1997; Rhein et al., 2002) and sequester carbon from the atmosphere to the deep ocean (Takahashi et al., 2009; Khatiwala et al., 2013). The production of this water mass, known as Labrador Sea Water (LSW; e.g. Clarke and Gascard, 1983; Lab Sea Group, 1998; Pickart et al., 2002), is influenced by air-sea heat fluxes and wind stress in the subpolar gyre, which vary in concert with the North Atlantic Oscillation (Hurrell, 1995; Våge et al., 2009). Convection in density space (diapycnal transformation) occurs both in the interior Labrador Sea and in the boundary current that circumnavigates it (Spall and Pickart, 2001; Pickart et al., 2002; Spall, 2004; Pickart and Spall, 2007), while overturning in depth space occurs only in the boundary current, where planetary geostrophic dynamics break down (Spall, 2010; Cessi and Wolfe, 2013).

The boundary current system that transports waters cyclonically around the Labrador Sea plays a crucial role in the production and export of LSW (Pickart 1992; Dickson and Brown, 1994; Cuny et al., 2002; Fischer et al., 2010). In particular, it is responsible for fluxing heat and freshwater to the interior basin (Prater 2002; Hátún et al., 2007; Lilly et al., 1999; Lilly and Rhines, 2002; Lilly et al., 2003) that then helps dictate the preconditioning of the water column to convection, as well as the restratification that occurs after the wintertime overturning (Lilly et al., 1999; Lilly and Rhines, 2002; Lilly et al., 2003; Katsman et al., 2004; Chanut et al., 2008; Gelderloos et al., 2011). The boundary current system is composed of three different branches. A coastal current, known as the West Greenland Coastal Current (Labrador Coastal Current), is found on the shelf on the eastern (western) side of the basin. This coastal current transports cold and fresh Arctic-origin and Greenland melt waters on the shelf (Fig. 1; Lin et al., 2018, Florindo-López et al., 2020). Offshore of the coastal current is the West Greenland Current (Labrador Current). This surface-intensified jet is tied to the shelfbreak and transports cold, fresh waters at the surface, and warm, saline, Atlantic-origin waters at depth (Colbourne et al., 1994; Rykova et al., 2015). The Atlantic-origin water mass (known as Irminger Water (IW); e.g. Lazier et al., 2002) is important due to its impact on stratification. While previous literature refers to the Labrador Coastal

* Corresponding author. 266 Woods Hole Road, Woods Hole, MA, 02543, USA.
E-mail address: apacini@whoi.edu (A. Pacini).

https://doi.org/10.1016/j.dsr.2021.103664
Received 29 April 2021; Received in revised form 30 August 2021; Accepted 3 November 2021
Available online 9 November 2021

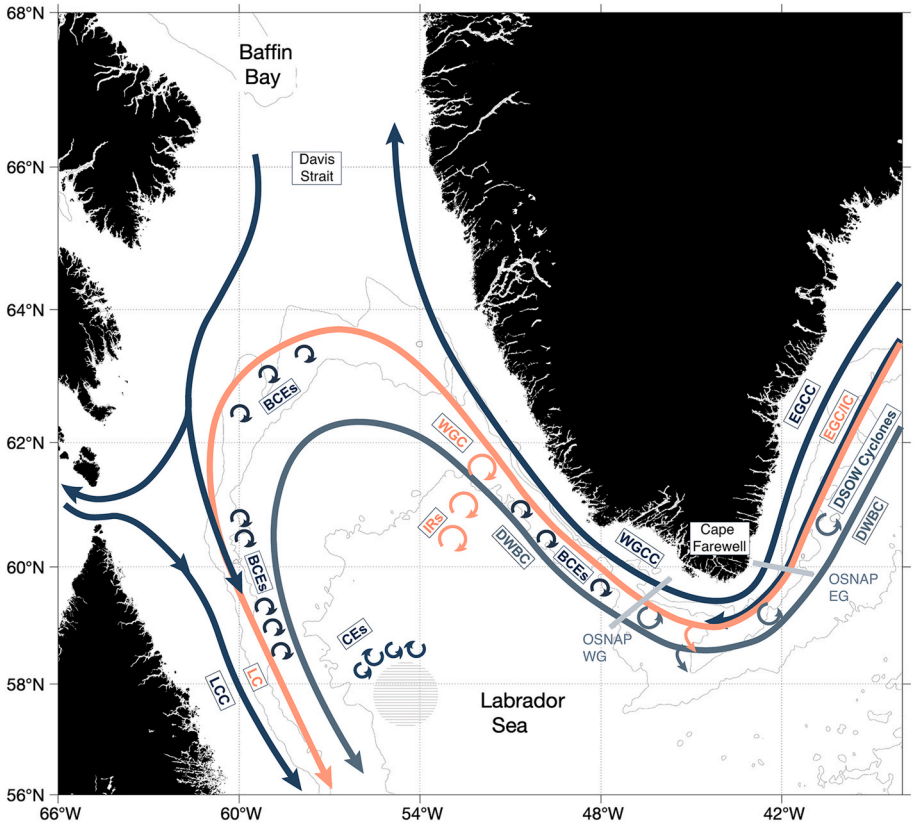

Fig. 1. Schematic circulation of the Labrador Sea. EGCC is the East Greenland Coastal Current; EGC/IC is the East Greenland Current/Irminger Current; DWBC is the Deep Western Boundary Current; WGCC is the West Greenland Coastal Current; WGC is the West Greenland Current; LCC is the Labrador Coastal Current; LC is the Labrador Current; DSOW Cyclones are Denmark Strait Overflow Water Cyclones; IRs are Irminger Rings; CEs are Convective Eddies; and BCEs are Boundary Current Eddies. The hatched area in the western/central Labrador Sea represents the area of deepest convection. Grey lines across the boundary current with OSNAP EG and WG labels indicate the locations of the OSNAP East and West Greenland mooring arrays, respectively.

Current as the inshore branch of the Labrador Current (e.g. Lazier and Wright, 1993), we follow the convention of Florindo-López et al. (2020) and refer to it as a coastal current, due in part to the governing dynamics differing between the offshore and inshore branches. Finally, the Deep Western Boundary Current (DWBC), centered near the 3000 m isobath, transports cold, dense overflow waters formed north of the Greenland Scotland Ridge that are advected around the subpolar gyre at depth (Dickson and Brown, 1994).

Observational and modeling studies have highlighted the high levels of eddy kinetic energy (EKE) found in the boundary current and interior Labrador Sea (e.g. Gascard and Clarke, 1983; Lilly et al., 1999; Eden and Böning, 2002; Prater, 2002; Lilly et al., 2003; Chanut et al., 2008). In particular, this EKE is a consequence of energetic mesoscale and submesoscale processes that can be divided into four main categories: (1) Irminger Rings (IRs), (2) Convective Eddies (CEs), (3) Boundary Current Eddies (BCEs), and (4) Denmark Strait Overflow Water Cyclones (DSOW Cyclones). While the first three features have a surface signature, the DSOW cyclones are mid-depth intensified. Models often overestimate the production of ventilated water in the Labrador Sea (Li et al., 2019), due to their inability to resolve these meso- and submesoscale processes. This large LSW production in models is in contrast with recent observations highlighting the eastern portion of the subpolar gyre as the dominant region for overturning, versus the Labrador Sea (Lozier et al., 2019). In a comparison between four models with differing resolution, Tagklis et al. (2020) demonstrated a linear dependence between vorticity fields (and associated frontogenesis) in the boundary currents and the production of LSW in the interior basin. As the model resolution increased, the vorticity in the boundary current increased, and the convected volume shrank, consistent with the notion that small-scale eddies from the boundary current are responsible for transporting buoyant water that limits the lateral extent of the convective patch (e.g. Rieck et al., 2019). Similarly, Pennelly and Myers (2020) compared eddy kinetic energy in a 1/60° model of the Labrador Sea with lower resolutions, emphasizing the importance of resolving eddies in order to properly quantify fluxes important for deep water formation. It is critical to understand the driving mechanisms behind this variability in order to accurately represent the production of dense water in climate models.

IRs are large (30–40 km), predominantly anticyclonic eddies shed from the West Greenland Current near 61 °N (Fig. 1), and transport IW southwestward (e.g. Lilly and Rhines, 2002; Lilly et al., 2003; Hátún et al., 2007; de Jong et al., 2016). While studies disagree as to their exact formation mechanism (whether it is baroclinic or barotropic instability), it is clear that they are an important source of buoyancy to the interior basin (e.g. Katsman et al., 2004; Gelderloos et al., 2011) and play a critical role in determining the location of the convective patch (e.g. Chanut et al., 2008; Tagklis et al., 2020). IRs have been observed from mooring data (de Jong et al., 2014), shipboard surveys (Rykova et al., 2009), glider transects (Hátún et al., 2007), and altimetry measurements (Prater, 2002; Lilly et al., 2003).

CEs are formed at the edge of the convective patch at the base of the mixed layer. Theoretical studies demonstrate that small-scale (on the order of the baroclinic deformation radius, < 10 km) cyclonic and anticyclonic features develop due to the baroclinically-unstable rim current around the convected region that acts to restratify the patch (Send and Marshall, 1995; Jones and Marshall, 1997; Lilly et al., 2003; Chanut et al., 2008). A small number of anticyclonic CEs have been observed with a mooring (Lilly et al., 2003), and modelling studies at high resolution have found their presence to have varying degrees of influence on the restratification process (e.g. Chanut et al., 2008; Gelderloos et al., 2011).

DSOW cyclones are formed as dense water cascades over the Denmark Strait sill and spins up cyclonic vorticity (Spall and Price, 1998). The features then propagate along the East Greenland slope (Bruce, 1995; von Appen et al., 2014), and, while previously thought to spin down in the Irminger Sea, they have recently been observed in the West Greenland boundary current system in mooring observations

(Pacini et al., 2021) and drifter tracks (Zou et al., 2021). The DSOW cyclones in the boundary current system can trap water and are responsible for a significant increase in overflow water transport as compared to non-cyclonic periods (Pacini et al., 2021). The ultimate fate of DSOW cyclones entering the Labrador Sea is unknown, as is their impact on the stratification of the interior.

Finally, BCEs are small-scale (order 10 km) features formed along the boundary between the West Greenland Current/Labrador Current and the interior due to baroclinic instability. Modeling studies with significantly high resolution (<1/12°) show the production of such features and associated levels of high EKE offshore of the boundary current system (Chanut et al., 2008; Gelderloos et al., 2011; Rieck et al., 2019). As wintertime convection continues in the interior Labrador Sea, the density gradient between the interior and the boundary current sharpens, which leads to increased baroclinic instability and the production of BCEs (Eden and Böning, 2002; Spall 2004; Gelderloos et al., 2011; Thomsen et al., 2014). These features are smaller, shallower, and less related to local topography than the Irminger Rings found in the northeastern corner of the Labrador Sea. The importance of BCEs in the heat and freshwater budget of the interior Labrador Sea is an active topic of research, as some modelling studies argue they play a critical role in controlling the extent of convection and the timing of restratification (Chanut et al., 2008), whereas other models indicate they are not important outside of the small area where the Labrador Current is adjacent to the convective patch (Gelderloos et al., 2011; Rieck et al., 2019). However, a fundamental knowledge gap exists in our understanding of BCEs, as they have never been observed.

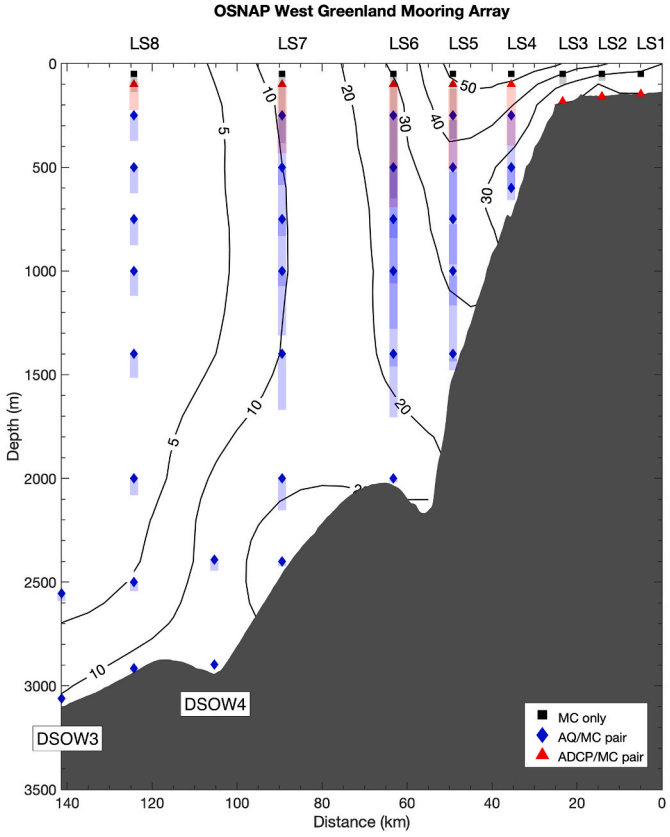

Fig. 2. Vertical section of instrumentation across the OSNAP WG mooring array. The names of the moorings are labeled and the bathymetry is plotted in grey (derived from a shipboard echosounder). LS1-LS3 are tripods on the shelf; LS4-LS8 are tall moorings; and DSOW4 and DSOW3 are short bottom-mounted moorings. Instrument types are identified in the legend: MC = MicroCAT; AQ = Aquadopp; and ADCP = acoustic Doppler current profiler. Shading indicates the range over which the individual instruments were blown down over the course of the two deployments. The contours indicate the four-year mean along-stream velocity outside of eddy periods. The horizontal axis origin, located on the far right of the vertical section, indicates the onshore-most grid cell of the gridded product (defined in the text).

In this study, we use four years of mooring data from the West Greenland shelf and slope to present the first observations of a meandering West Greenland Current (WGC) and argue that this meandering generates BCEs. The structure of the paper is as follows. The data and methods are presented first, and the statistics and structure of the mesoscale features are subsequently characterized. Following this, the question of whether the features are coherent anticyclones or meanders is investigated. Formation mechanisms are then addressed, and the seasonality of the instability is documented. Finally, implications for the interior heat budget of the Labrador Sea are considered, long-term trends are investigated, and the relationship with downstream IR production is explored.

2. Data and methods

2.1. Mooring data

A high-resolution mooring array was deployed in the West Greenland boundary current system as part of the Overturning in the Subpolar North Atlantic Program (OSNAP; Lozier et al., 2017; Lozier et al., 2019) (Figs. 1 and 2). The moorings were deployed in 2014 and have been serviced every two years. In this study we use the first four years of hourly data. The array consists of ten moorings (Fig. 2): three tripods on the shelf (moorings LS1-LS3), five tall moorings located between the 500 m and 3000 m isobaths (moorings LS4-LS8), and two short bottom-instrumented moorings in the DWBC (moorings DSOW3-4). A total of 49 Sea-Bird Scientific MicroCATs recorded pressure, temperature, and conductivity, 33 Nortek Aquadopps recorded pressure and zonal and meridional velocity components, and 3 75-kHz Long-Ranger acoustic Doppler current profilers (ADCPs) (LS1, LS2, and LS3) and 5 300-kHz Workhorse ADCPs (LS4 through LS8) measured pressure and velocity profiles in the upper part of the water column. The data and processing are described in detail in Pacini et al. (2020). Hourly gridded vertical sections of different variables were constructed by Pacini et al. (2020); both the individual instrument data and the gridded product will be used in this study. The velocity data have been rotated into an alongstream and cross-stream coordinate system which minimizes the integrated cross-stream velocity, and the data were de-tided using the harmonic tidal routine T_Tide (Pawlowicz et al., 2002). Positive along-stream velocity (u) is oriented parallel to the isobaths towards the northwest (318 °T), and positive cross-stream velocity (v) is directed offshore perpendicular to the isobaths, towards the southwest. The gridded product, computed using a Laplacian-spline interpolator (Smith and Wessel, 1990) has a resolution of 100 m in the vertical and 5 km in the horizontal (Pacini et al., 2020).

2.2. Satellite data

Satellite data are used in parts of the study. Level 2 Modis 4 μm Aqua and Terra nighttime sea surface temperature (SST) data are used to investigate along-track SST variability at a nadir resolution of 1 km (Brown and Minnett, 1999). The data are provided with a data quality flag, which uses sharp gradients to detect the presence of clouds. However, given the strong temperature gradients between the West Greenland Coastal Current (WGCC) and WGC, the algorithm tends to over-reject pixels near the frontal zone of interest to this study. Following von Appen et al. (2014), a modified processing algorithm is applied, such that temperatures between -2 °C and 12 °C are retained. Sutherland et al. (2013) have shown that sea surface temperature data and observed ocean temperatures remain correlated down to 200 m in the region near Cape Farewell. Only periods when 75% of the region of interest (53°N–68°N, 35 °W–69 °W) is not cloud-covered are considered. Based on this criterion, 40% of the time the region is cloud-covered and

does not return a useable satellite pass.

The daily, gridded surface altimetric data product provided by the EU Copernicus Marine Service (CMEMS) is used to investigate surface geostrophic velocities and eddy kinetic energy (EKE) (as in Rieck et al., 2019). The lateral resolution of the grid is 0.25° and the time period considered is January 1, 2014 to January 1, 2019. EKE is calculated as

$$EKE = 0.5\left(u'^2 + v'^2\right) \quad (1)$$

where primes indicate deviations from the corresponding yearly mean, in order to avoid the influence of long-term trends on the calculation of EKE (e.g. Penduff et al., 2004; Rieck et al., 2015; Rieck et al., 2019).

2.3. Feature detection method

Instances of enhanced mesoscale activity in the boundary current are identified using a graphical user interface (GUI). The GUI is described in detail in Pacini et al. (2021) who used it to characterize DSOW cyclones at the array location. At each hourly timestep, three days of mooring data (depth vs. time) are visualized for the moorings seaward of the shelfbreak, and the user selects instances of mesoscale activity by the mooring number, nature (cyclonic feature, anticyclonic feature, or dipole pair—which is an anticyclonic feature immediately followed by a cyclonic feature), and start and stop times. The user also selects the center of the feature. Instances of such mesoscale activity are identified for all four years for moorings LS5, LS6, LS7, and LS8 (there was no pronounced signal of these features at mooring LS4).

3. Results

3.1. Statistics and structure of anticyclonic features and dipole pairs

Using the GUI described in section 2.3, instances of enhanced mesoscale activity in the boundary current were identified. Abundant anticyclonic features, as well as dipole pairs, were observed within the core, and just offshore, of the WGC. Distinct from this, cyclonic features were observed offshore of the WGC, near 2000 m at mooring LS6. The latter are the DSOW cyclones referred to above that are presented in Pacini et al. (2021). Here we focus on the anticyclonic features and dipole pairs.

A total of 147 anticyclonic features and 54 dipole pairs were identified, which together account for 31% of the four-year record (Fig. 3). The anticyclones were predominantly observed at LS5 (123 at LS5, 24 at LS6), at the location of the core of the mean WGC (Fig. 2), while the dipole pairs were more often sampled at LS6 (13 at LS5, 41 at LS6), offshore of the mean core location of the WGC (Fig. 2). The dipoles are composed of a leading anticyclone and a trailing cyclone. We created an index, referred to as the meander index, to quantify the variation in feature presence over the four-year record, defined as the 28-day low-pass of the feature identification logical. This lowpass converts the logical (a binary value of 1 or 0, corresponding to presence or absence of features, respectively) to a timeseries with values between 0 and 1 that indicate sustained periods of anticyclonic or dipole pair activity (Fig. 3c). Note in Fig. 3c that there are three periods of enhanced activity that generally occurred during the winter/spring of 2016, 2017, and 2018.

Fig. 4 shows a Hovmöller plot of the monthly mean eddy kinetic energy (EKE) of the WGC at 300 m. This reveals that the winter/spring time period of all four years exhibited elevated EKE (as high as 300 cm^2/s^2). The peak in the timing of this EKE maximum shifts between years, as does the magnitude and duration of elevated variability. In 2016 and 2018, the peak in EKE occurs between January and April, while in 2017 the period of elevated EKE extends through June. This is true as well for the presence of anticyclones/dipole pairs (Fig. 3), which shows enhanced feature activity as identified by the GUI between Jan and April in 2016 and 2018, and a longer period of enhanced activity between January and June in 2017. The EKE signature in winter/spring 2015 is less extensive, which is the year when there was no enhanced feature presence. This is addressed further in Section 3.3.3.

Using the identified anticyclonic features, a composite feature was created in order to diagnose its structure and composition. All of the features took approximately 60 h to transit past the mooring array, thus time normalization was not necessary. The individual features were

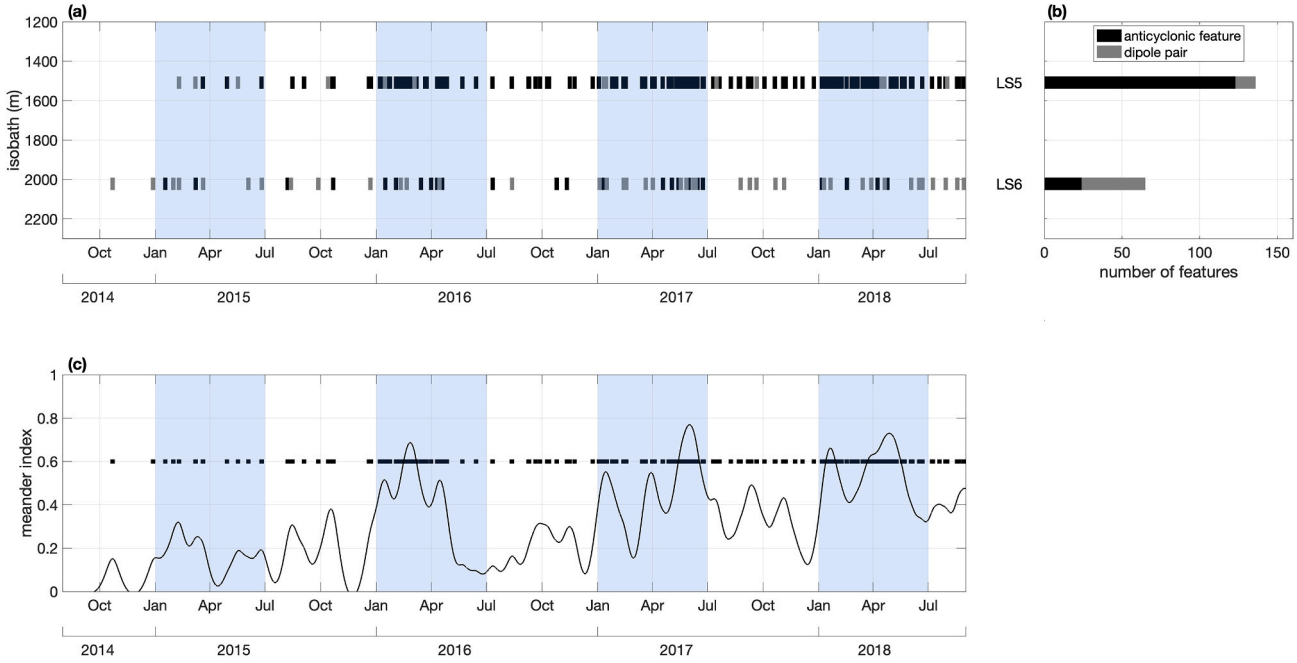

Fig. 3. (a) Statistics of anticyclonic and dipole features observed at moorings LS5 and LS6 over the four years of data. Black bars indicate anticyclonic features; grey bars indicate dipole pairs. (b) Histogram of features at LS5 and LS6. (c) Timeseries of the meander index (black line; defined as the 28-day lowpass of the feature identification logical) with individual features (both anticyclonic and dipole features) denoted by the black squares. The time period Jan-Jul is indicated each year (blue shading).

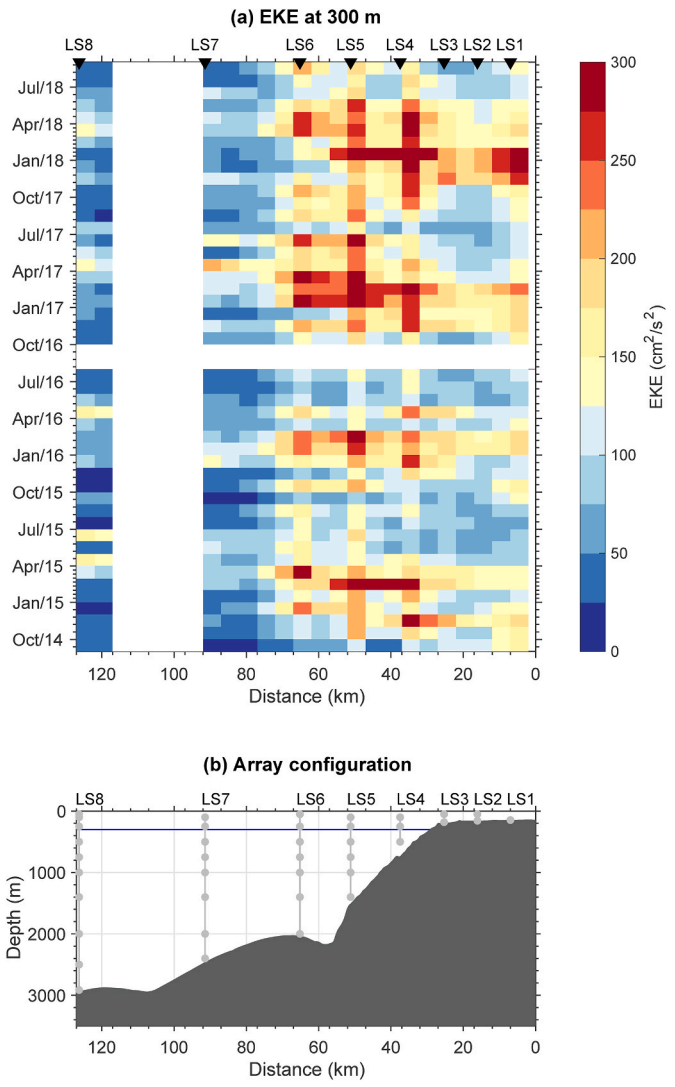

Fig. 4. (a) Monthly eddy kinetic energy at 300 m as a function of time and distance across the array. (b) Mooring array configuration in the vertical. The blue line indicates the depth of the EKE timeseries in (a).

aligned along their center time, and an average was taken along this time axis. Seven features were excluded from the composite that occurred very close to nearby features (one in each pair was retained). The resulting composite anticyclone at LS5, constructed using 116 features, is shown in Fig. 5. This reveals that, as the features pass by, there is a bowling of the isopycnals between the surface and 1000 m, a slight reduction in along-stream flow, and a reversal in the cross-stream velocity from onshore (negative v) at the leading edge to offshore (positive v) at the trailing edge. Using the along-stream flow averaged between the surface and 700 m (thus the core of the features) to convert the time axis to a distance axis, a characteristic length scale of 20 km is derived.

The composite anticyclonic feature at LS6, constructed using 24 instances (none were excluded) and shown in Fig. 6, exhibits the same bowling of isopycnals between the surface and 1000 m depth as the anticyclonic feature at LS5, but instead exhibits an intensification in the along-stream velocity over this depth range. The reversal in cross-stream velocity follows the same pattern as the feature at LS5. The leading anticyclone from the dipole pairs has the same structure as the composite anticyclonic feature at LS6 (not shown). The trailing cyclone does not have a distinctive hydrographic signature, and is instead reflective of the ambient temperature/salinity structure.

3.2. Meanders or coherent eddies?

We now argue that the features identified by the GUI predominantly reflect meandering of the WGC rather than the passage of coherent eddies. This is based on several lines of evidence. First of all, if the features were discrete eddies then one would expect to see evidence of oppositely signed azimuthal flow at successive moorings. However, of the 123 anticyclones sampled at LS5, only 14 produced negative along-stream flow at mooring LS4, as would be expected of a coherent eddy. We hasten to say that the spacing between these two moorings is 15 km, while the deduced diameter of the features from the composite is 20 km. As such, if discrete eddies were passing by the array over a range of cross-stream locations, it is likely that LS4 would sometimes miss the onshore signature. Nonetheless, such a small percentage of cases with return flow (11%) implies that coherent eddies were not the dominant process being measured.

To shed more light on this we consider the Ertel potential vorticity Π, calculated using the gridded product as:

$$\Pi = \frac{f}{g}\frac{\partial b}{\partial z} - \frac{1}{g}\frac{\partial u}{\partial y}\frac{\partial b}{\partial z} + \frac{1}{g}\frac{\partial u}{\partial z}\frac{\partial b}{\partial y}, \quad (2)$$

where u is the along-stream velocity, b is the buoyancy term, f is the Coriolis term, y is the cross-shelf direction, and z is the vertical coordinate (e.g. Pickart et al., 2005; Spall and Pedlosky, 2008; Lin et al., 2018). The buoyancy is $b = -g\rho/\rho_o$, where ρ is the density, ρ_o is the reference density, and g is the gravitational acceleration. The first term in (2) represents the stretching vorticity, the second term represents the relative vorticity, and the third term represents the tilting vorticity. Each term is smoothed using a 3-h temporal filter and a 300 m vertical filter. We note that this formulation of Π does not account for variations in vorticity in the downstream direction. Given the two-dimensional nature of the mooring array, it is not possible to estimate $\frac{\partial v}{\partial x}$. However, we explored the role of this term using an idealized representation of a feature progressing past a mooring array. At both LS5 and LS6, the full relative vorticity is qualitatively similar to the $\frac{\partial u}{\partial y}$ term; thus, our conclusions are not impacted by this limitation.

The four-year mean vertical section of the ratio of relative vorticity to stretching vorticity (ζ/f, where $\zeta = \frac{\partial u}{\partial y}$) across the array, in the absence of mesoscale activity, is shown in Fig. 7. This nicely reveals the expected regions of positive and negative ζ/f in the WGC: the offshore edge of the WGC is associated with cyclonic relative vorticity (positive ζ/f), while the onshore side of the WGC is associated with anti-cyclonic relative vorticity (negative ζ/f). The zero-contour is located at the core of the WGC near LS5. Using the hourly gridded product of ζ/f, an analogous time-depth composite was constructed of the relative vorticity at the grid point closest to mooring LS5 for the 116 anticyclonic features comprising the composite anticyclone at that mooring (Fig. 5b). This reveals that, outside of the feature, the relative vorticity is close to zero, while during the passage of the feature ζ/f becomes strongly negative. Simultaneously, the along-stream velocity is reduced (Fig. 5c).

The situation is markedly different at mooring LS6. In the mean this mooring is situated in the region of positive relative vorticity on the offshore side of the WGC (Fig. 7). The analogous composite of ζ/f at the grid point closest to LS6 for the 24 anticyclones passing that mooring shows that, on either side of the feature, the relative vorticity is positive, while at the core of the feature ζ/f is close to zero (Fig. 6b). Simultaneously, the along-stream velocity is enhanced (Fig. 6c). As such, the vorticity composites at both moorings are consistent with an offshore shift of the WGC; i.e., a leftward shift of the vorticity field of Fig. 7. In particular, the region of negative vorticity previously situated at mooring LS4 is now located at LS5, while the region of near-zero relative vorticity previously situated at LS5 has moved to LS6. This is indicative of a meandering WGC.

At the same time, if these were coherent anticyclones, one would

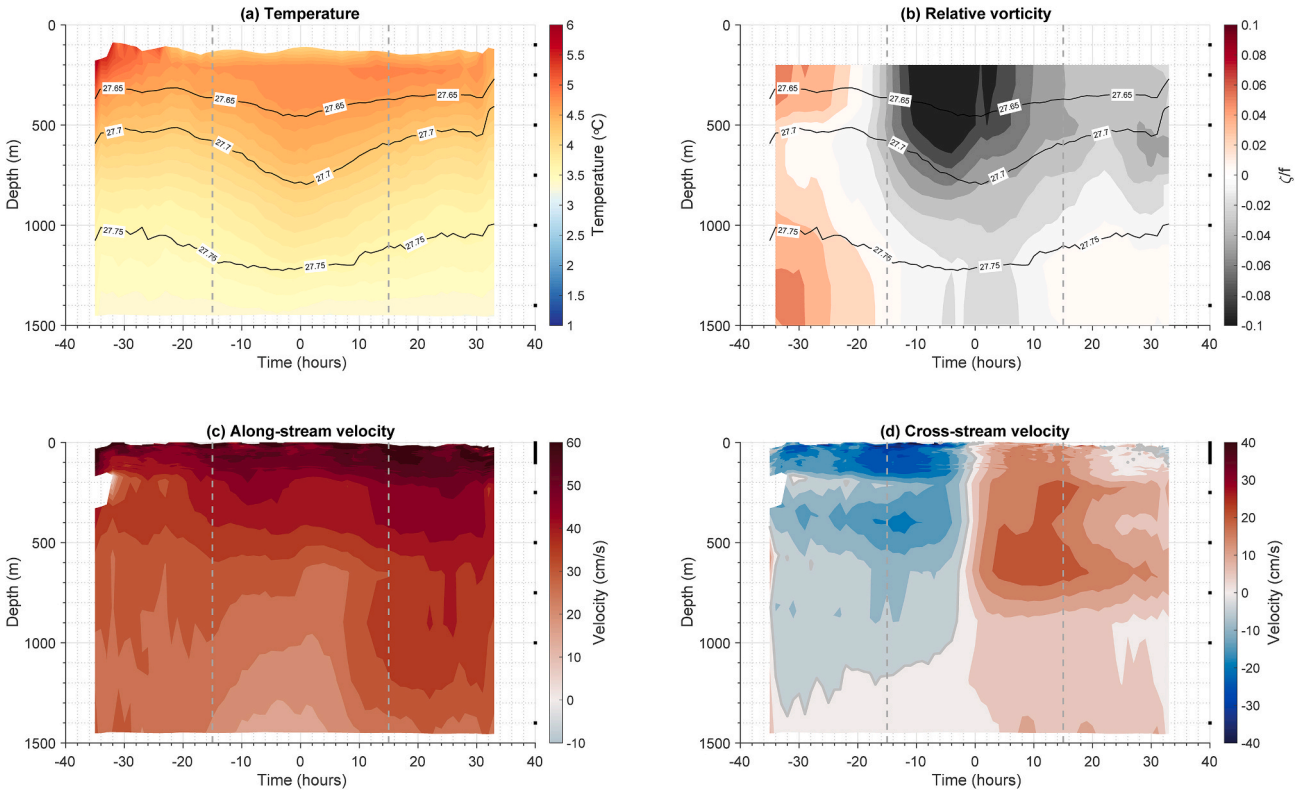

Fig. 5. Composite anticyclonic feature at LS5. The composite is made up of 116 features. (a) Temperature, plotted as a function of depth and time (hours) from the center of the feature (at 0 h), with isopycnals contoured every 0.05 kg/m^3. Negative time indicates the leading edge, positive time indicates the trailing edge. (b) Same as (a) but for the ratio of relative vorticity to stretching vorticity (ζ/f). (c) Along-stream velocity. (d) Cross-stream velocity. Black squares indicate nominal instrument depths. The vertical dashed lines bracket the core of the feature.

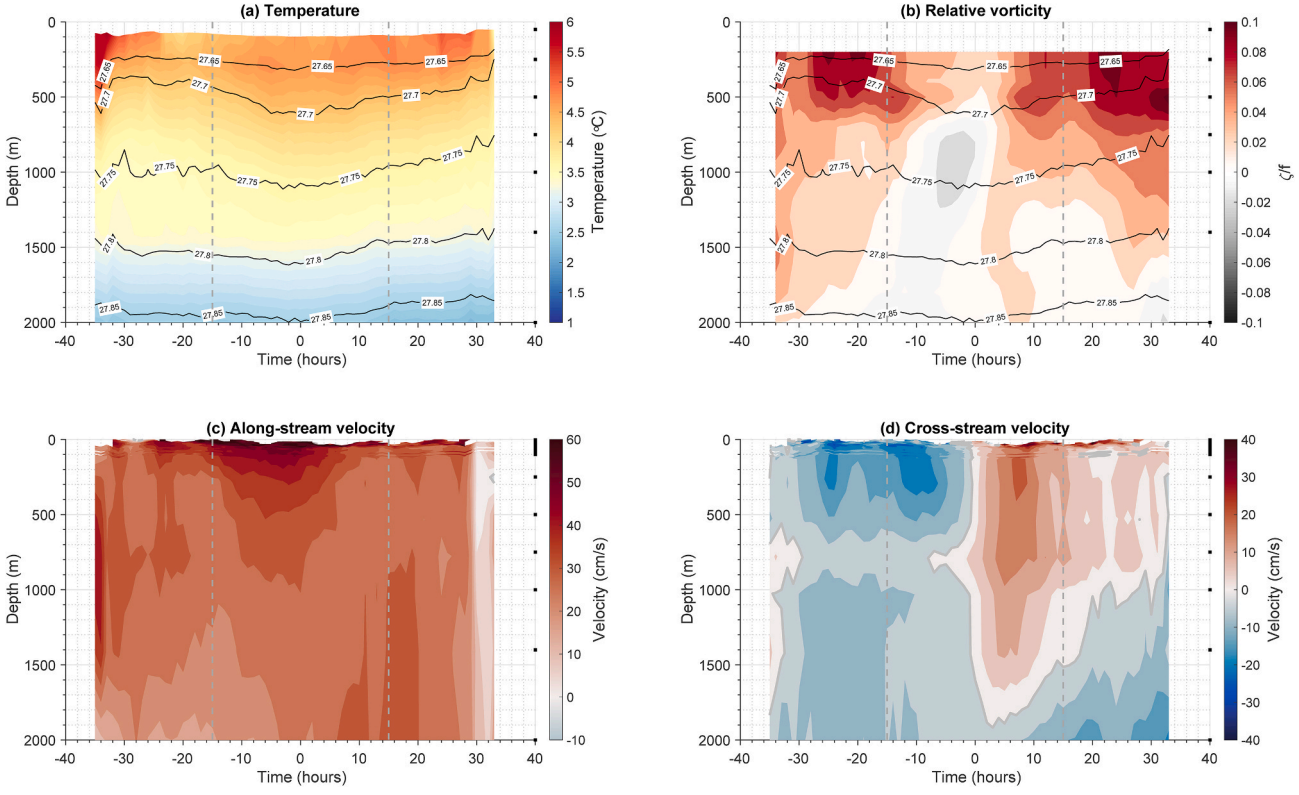

Fig. 6. Same as *Fig. 5* but for LS6. The composite is made up of 24 features.

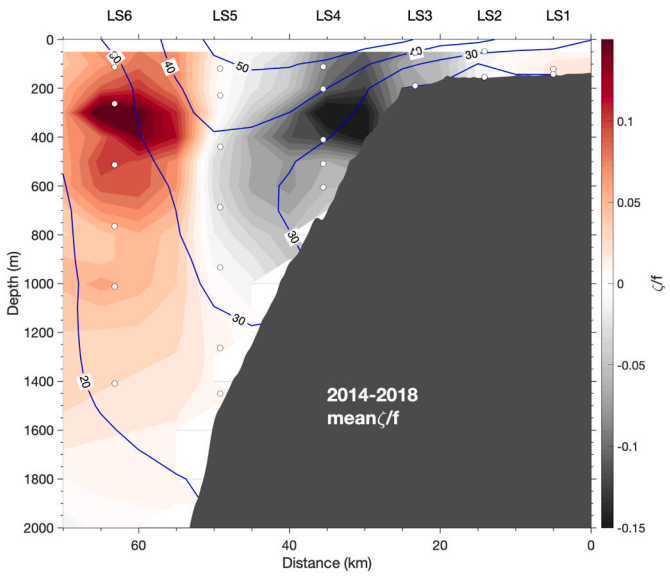

Fig. 7. Mean vertical section of the ratio relative vorticity to stretching vorticity (ζ/f) in the absence of mesoscale activity between 2014 and 2018. The mean along-stream velocity in the absence of mesoscale variability is contoured. See text for details on calculation of ζ.

expect them to impinge on a particular mooring in a variety of different ways—i.e., they could be sampled directly through their center, or could pass onshore or offshore of the mooring. Depending on which of these cases applies, the along-stream velocity measured by the mooring would either stay the same, increase, or decrease. This in turn would result in an ill-defined along-stream velocity composite, with the varied impingement angles and associated along-stream velocity profiles averaged together. This is in contrast to the robust composites presented above. We note that in their analysis of coherent Denmark Strait Overflow Water cyclones passing by the OSNAP WG array, Pacini et al. (2021) developed a methodology for identifying centered eddies for a given mooring. This technique did not work in the present case of the anticyclonic features, further suggesting that they are not discrete eddies.

Additional evidence of meandering is provided by the high-resolution (order 1 km) satellite SST data. While cloud cover in the region is present roughly 40% of the time (see section 2.2), we inspected every good satellite pass during the four-year mooring deployment and found sustained evidence of meanders of the SST front associated with the WGC. At the same time, there were only limited instances of discrete eddies. An example of an image revealing meanders is shown in Fig. 8a, where the 3 °C contour corresponds to the center of the surface front associated with the WGC in winter. This particular example, on December 24, 2015, coincided with the detection of an anticyclonic feature at LS5 and a dipole pair at LS6. The repeated cusping of the 3 °C isotherm near 59 °N is the surface representation of this train of features. A series of three good passes at this time over the course of 6 h, shown superimposed in Fig. 8b, provided the ability to track the propagation of this cusping front, and a velocity of 50 cm/s was deduced. This compares well to the propagation velocity of ~50 cm/s of the particular feature identified at LS5 during the same period, where this velocity is the maximum velocity observed by the mooring array (at LS5 and LS6) during the passage of the feature. Additionally, the length scale of the cusping in the SST front is order 25 km, consistent with the derived wavelength of the anticyclonic features in the mooring record of 20 km. It is important to recall that it is rare for the mooring array to sample a feature at more than one mooring at a given timestep. This can be seen in Fig. 3a, where features at LS5 tend to appear at different times than features at LS6. This is because the spacing between LS4, LS5, and LS6, is 14 km and thus a 20 km feature has only a slight chance of impinging on more than one mooring.

Finally, the fact that anticyclonic features were predominantly observed at LS5 while dipole pairs were mainly measured at LS6 represents further evidence that the features are meanders. As shown schematically in Fig. 9, when the WGC meanders offshore, a mooring at the mean location of its core (LS5) would only observe a train of features with anticyclonic rotation. By contrast, at a mooring offshore of the mean WGC (LS6), a meander would appear as a dipole pair where the leading feature has anticyclonic rotation and the trailing feature has cyclonic rotation. Given that features are not observed onshore of LS5, we suspect that the boundary current cannot meander onshore of LS5 due to the steep topography in this region, as was the case in a numerical model of the shelfbreak jet in the Beaufort Sea (Spall et al., 2008). A similar asymmetry is observed in the Agulhas Current, where submesoscale meanders are observed only on the offshore side of the jet and are hypothesized to be topographically-constrained (Elipot and Beal, 2015).

Cimoli et al. (2017) used a model shelfbreak jet to derive a parameter space that distinguishes between regions of stable flow, meandering flow, and eddying flow. The parameter space is a function of γ, which is a measure of the baroclinicity of the flow, and T_p, which is a measure of the bottom topography, WGC speed, and stratification. Specifically,

$$\gamma = \frac{H_{jet}}{H - H_{jet}} \tag{3}$$

$$T_p = \frac{-sfR_d^2}{HU_{max}}, \tag{4}$$

where H_{jet} is the depth of the jet, H is the bottom depth, s is the topographic slope, R_d is the baroclinic Rossby radius, f is the Coriolis term, and U_{max} is the maximum velocity of the jet. We estimated the values of γ and T_p for the WGC using the four-year mean vertical sections of along-stream velocity and buoyancy frequency. Error bars were estimated by considering a range of values for the depth of the jet (450–550 m) and choosing different averaging regions for the stratification. Based on this, we calculate a γ of 0.5 ± 0.08 and a T_p of -.15 ± 0.07; thus, the WGC is found to be near the edge of the theoretical meandering and eddying regimes.

Given the various lines of evidence presented above, we conclude that the features observed at the OSNAP WG mooring array are meanders of the WGC, and that they are on the verge of breaking off to become anticyclonic eddies. Indeed, it is likely that the 14 features displaying negative along-stream flow at mooring LS4 onshore of the core of the WGC represent instances of detached eddies from the boundary current, i.e. the BCEs described in the modeling literature.

3.3. Formation mechanism

Modeling studies have addressed the formation mechanisms responsible for the production of eddies along a rim current. For example, Spall (2004) documented the development of boundary current eddies within a circular domain with a warm boundary current progressing cyclonically around a cold interior basin (meant to represent the Labrador Sea). In that analysis, Spall (2004) demonstrated that small-scale BCEs are formed all along the front due to baroclinic instability as the density gradient between the interior and the boundary current is sharpened during wintertime convection. This process results in offshore transport of heat from the boundary current to the interior basin, which ultimately contributes to restratification in the interior after convection.

Other modeling studies similarly describe the connection between an accelerating boundary current and the production of BCEs (e.g. Chanut et al., 2008; Gelderloos et al., 2011; Rieck et al., 2019). de Jong et al.

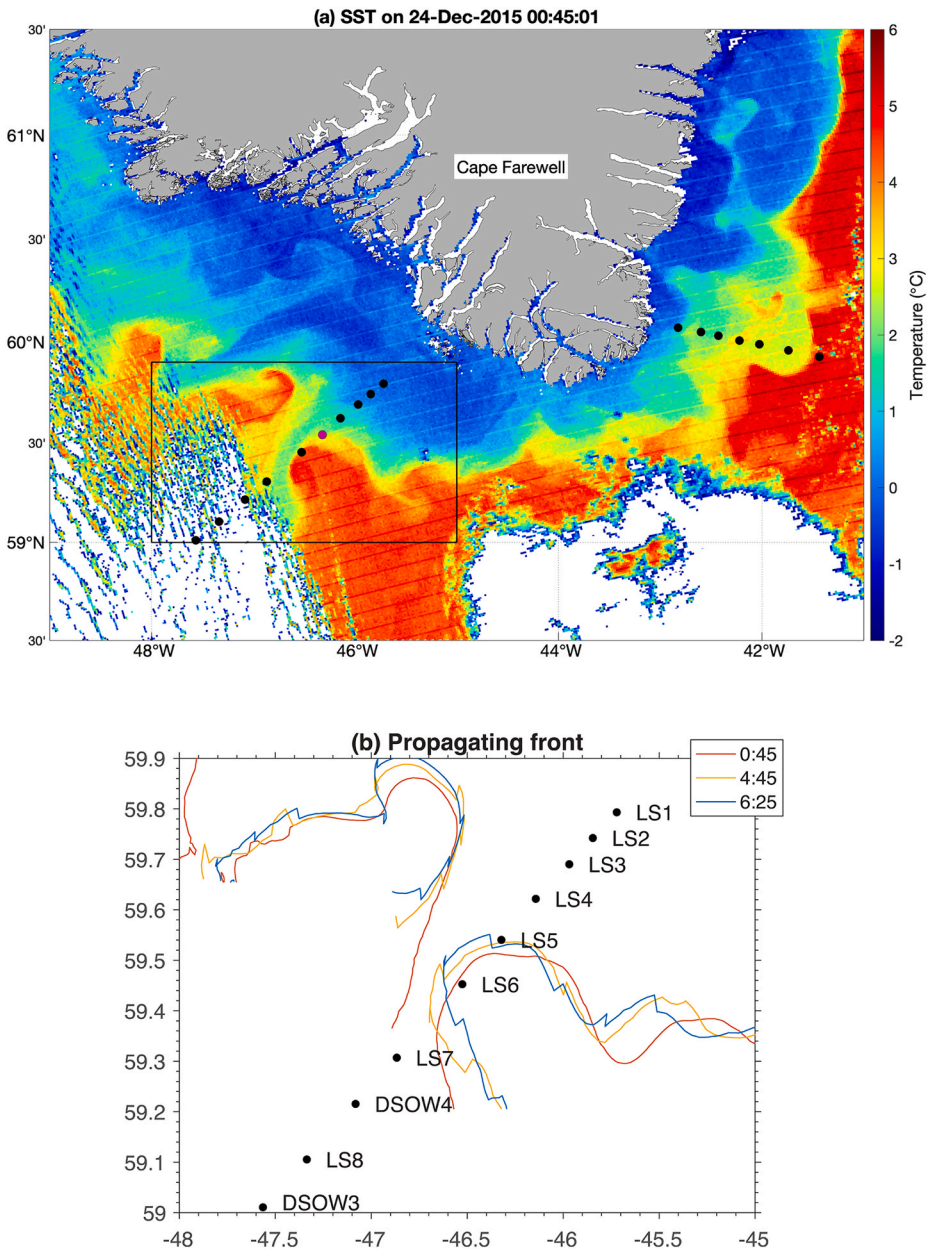

Fig. 8. (a) Example SST pass from December 24, 2015 illustrating a meandering front at the OSNAP WG mooring array (black circles). The satellite pass, coincided with the detection of an anticyclonic feature at LS5 (purple circle) and a dipole pair at LS6. Note the data are not contoured, and instead plotted at their native resolution. (b) Evolution of the 3 °C isotherm over the course of three consecutive satellite passes within the box in (a), smoothed over 5 pixels. The time of each pass is indicated in the legend.

(2016) demonstrated that in the 1/12° configuration of the Family of Linked Atlantic Models Experiment (FLAME), the variability in boundary current density was double that of the interior density, and thus was primarily responsible for the changes in the density gradient between boundary current and interior. Using a combination of model output and data in the Labrador Current (LC; Fig. 1), Thomsen et al. (2014) performed a linear stability analysis and found that three instability modes exist in the LC. They found that an interior mode, best explained by baroclinic instability with maximum growth rates of 1 day^{-1}, can explain the observed wintertime enhancement of EKE in the LC. Is baroclinic instability the formation mechanism responsible for the generation of WGC meanders, and, if so, does it have a seasonal signal?

3.3.1. *Instability of the WGC*

To investigate the processes involved in generating the meanders, we first checked to see if the WGC meets the necessary criteria for barotropic and baroclinic instability. Barotropic instability is responsible for the conversion of mean kinetic energy to eddy momentum flux (Spall et al., 2008) and is dampened by steep bathymetry and aided by strong horizontal velocity gradients (von Appen et al., 2016). Specifically, the value of $\beta - \partial^2 u/\partial y^2$ must change sign within the domain, where β is topographic beta, u is the along-stream velocity, and y is the cross-stream direction (e.g. Vallis, 2006). The OSNAP WG mooring data reveal that the boundary current meets this criterion in all months of the year (not shown). However, a metric for the tendency of the boundary current to exhibit barotropic instability is the ratio of the relative vorticity to the stretching vorticity (a measure of the Rossby number). If this ratio exceeds 0.5, then it is likely the boundary current is barotropically unstable (e.g. Pickart et al., 2005; Lin et al., 2018). For the hourly sections of the WGC, this ratio never exceeds 0.5 (max value 0.45), and the four-year mean value is ~0.1 (Fig. 7).

Baroclinic instability results in the conversion of mean available potential energy to eddy density flux (Spall et al., 2008) and is dampened by stratification and aided by vertical shear of the horizontal velocity (von Appen et al., 2016). A necessary, but not sufficient, criterion for baroclinic instability is that the gradient of total Ertel potential vorticity, $\partial\Pi/\partial y$, change sign within the domain. The WGC satisfies this criterion for all months (not shown).

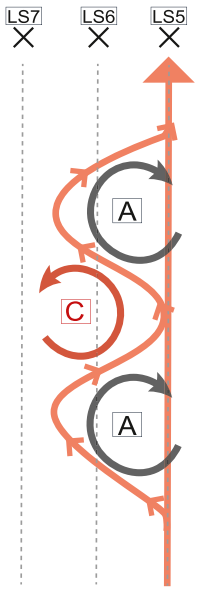

Fig. 9. Schematic depicting the evolution of a meander past moorings LS5, LS6, and LS7 as viewed from the surface. The mean flow is represented by the straight arrow at LS5. The meandering is shown by the sinusoidal orange curve. The dashed lines indicate the location that each mooring samples over time. The black circles indicate anticyclonic features, and the red circle indicates a cyclonic feature in the dipole train at LS6.

Given that the boundary current meets the necessary criteria for both barotropic and baroclinic instability, we now perform an energetics analysis following Spall et al. (2008) to diagnose the relative importance of these instabilities to the meandering of the WGC. The baroclinic conversion term represents conversion from mean available potential energy to eddy energy following:

$$P = -\frac{1}{2} g\overline{\rho}^2 (\rho_{0z})^{-1} \tag{5}$$

$$BC = -g\gamma\overline{v'\rho'}\,, \tag{6}$$

where P is the mean available potential energy, ρ is the deviation of the density profile from the mean density profile outside the WGC (ρ_0) (see also von Appen and Pickart, 2012), ρ_{0z} is the vertical gradient of the density outside the WGC, $\gamma = \partial z/\partial x$ is the isopycnal slope, and $\overline{v'\rho'}$ is the eddy density flux. Overbars denote the time mean, and primes denote the deviations from the mean.

The barotropic conversion term represents conversion from mean kinetic energy to eddy energy following:

$$K = -\frac{1}{2}\rho_0(\overline{u}^2 + \overline{v}^2) \tag{7}$$

$$BT = \overline{v'u'}U_y\rho_0\,, \tag{8}$$

where K is the mean kinetic energy, ρ_0 is the density profile outside the boundary current, u is the along-stream velocity, v is the cross-stream velocity, $\overline{v'u'}$ is the eddy momentum flux, and U_y is the cross-stream gradient of the mean along-stream flow (Spall et al., 2008; von Appen et al., 2016; Håvik et al., 2017; Huang et al., 2019).

Using these equations, the different energetics terms were calculated using the hourly gridded fields for the four years of mooring data. The resulting vertical sections are displayed in Fig. 10. The region of greatest mean available potential energy is where the isopycnals exhibit the steepest slopes, in the core of the WGC. The eddy density flux is negative throughout the water column, indicating the transfer of lighter water from the inshore side of the boundary current to the offshore side (i.e., positive v', negative ρ'). The associated baroclinic conversion is positive throughout the upper portion of the WGC, with particularly strong conversion at LS4 inshore of the core of the WGC (Fig. 10 a-c).

The mean kinetic energy of the boundary current is largest in the core of the WGC, with a positive eddy momentum flux on the offshore side of the WGC and a negative eddy momentum flux on the inshore side of the WGC. This indicates that when the WGC shifts offshore (positive v') the boundary current is stronger at LS5/LS6 (positive u') and weaker at LS4 (negative u'). This is consistent with the meandering of the WGC diagnosed above. The barotropic conversion is positive offshore of the WGC and negative onshore of the WGC, but significantly weaker than the baroclinic conversion (Fig. 10 d-f). The order of magnitude difference between the two conversion terms indicates that baroclinic instability is the dominant mechanism responsible for the formation of the WGC meanders.

3.3.2. *Seasonality of the instability*

Recall that the meandering of the WGC is seasonal in nature. What causes the seasonality in the baroclinic instability that drives this? To investigate this question, we revisit the meander index defined above in section 3.1. This is compared to the average EKE computed at 300 m depth between LS5 and LS6 (lowpassed with the same 28-day filter) in Fig. 11a. The correlation between these two timeseries is high (0.64) and statistically significant ($p < 0.01$). This confirms that the periods of elevated meander activity are, in fact, correlated with periods of enhanced WGC EKE, as was suggested by the EKE evolution of the WGC shown in Fig. 4. It should be noted that the EKE of the WGC is significantly baroclinic, with ratios of ~3 when the EKE at 300 m is compared with EKE at 1500 m. This shear in EKE indicates that variability of the boundary current has a tendency to be surface-intensified, as would be expected for the production of baroclinic eddies (von Appen et al., 2016).

Eady (1949) calculated the e-folding growth rate ω for a two-layer flow in the quasi-geostrophic limit as a function of Richardson number, $Ri = N^2/S^2$, where $N^2 = \frac{-g}{\rho}\frac{\partial\rho}{\partial z}$ is the square of the buoyancy frequency and $S^2 = \left(\frac{\partial u}{\partial z}\right)^2 + \left(\frac{\partial v}{\partial z}\right)^2$ is the square of the shear. Using the thermal wind relation, Stone (1970) provided a modification to the growth rate for cases where stratification is weak. The modified Eady growth rate is defined as $\omega^2 \cong 0.09f^2/(1 + Ri)$, where f is the Coriolis parameter. In a model of the LC, this growth rate was found to be 1 day^{-1} in winter and 0.2 day^{-1} in summer (Thomsen et al., 2014).

To compute ω for the WGC, the gridded mooring data were used to calculate the stratification N^2 and shear S^2, and hence Ri. This was done for each hourly timestep. For the purposes of this analysis, the values between LS5 and LS6 at 300 m are averaged together, and the hourly growth rate and 28-day lowpassed growth rate are shown in Fig. 11b in relation to the meander index. The timeseries of ω exhibits periods of large growth rate (1-1.5 day^{-1}) during the winter/spring, roughly coincident with periods of enhanced meandering activity. The correlation coefficient between the meander index timeseries and the baroclinic growth rate is 0.58 ($p < 0.01$).

We note that when N^2 is small, S^2 is large and vice-versa; thus, the shear acts in concert with the stratification to increase or decrease the Richardson number of the WGC. However, the mooring data indicate that the stratification is an order of magnitude larger than the shear, as is its variability, and thus drives the changes in the baroclinic growth rate. Hence, the seasonal changes in the stratification of the WGC are responsible for the wintertime tendency for meanders to develop. The next question is, what causes the seasonal changes in stratification?

As demonstrated by Pacini et al. (2020), using the same mooring data presented in this study, the two main water masses in the WGC are the LSW and IW, which together dictate the stratification of the water column. LSW is the weakly stratified winter product formed by convection in the interior Labrador Sea, within the boundary current in the

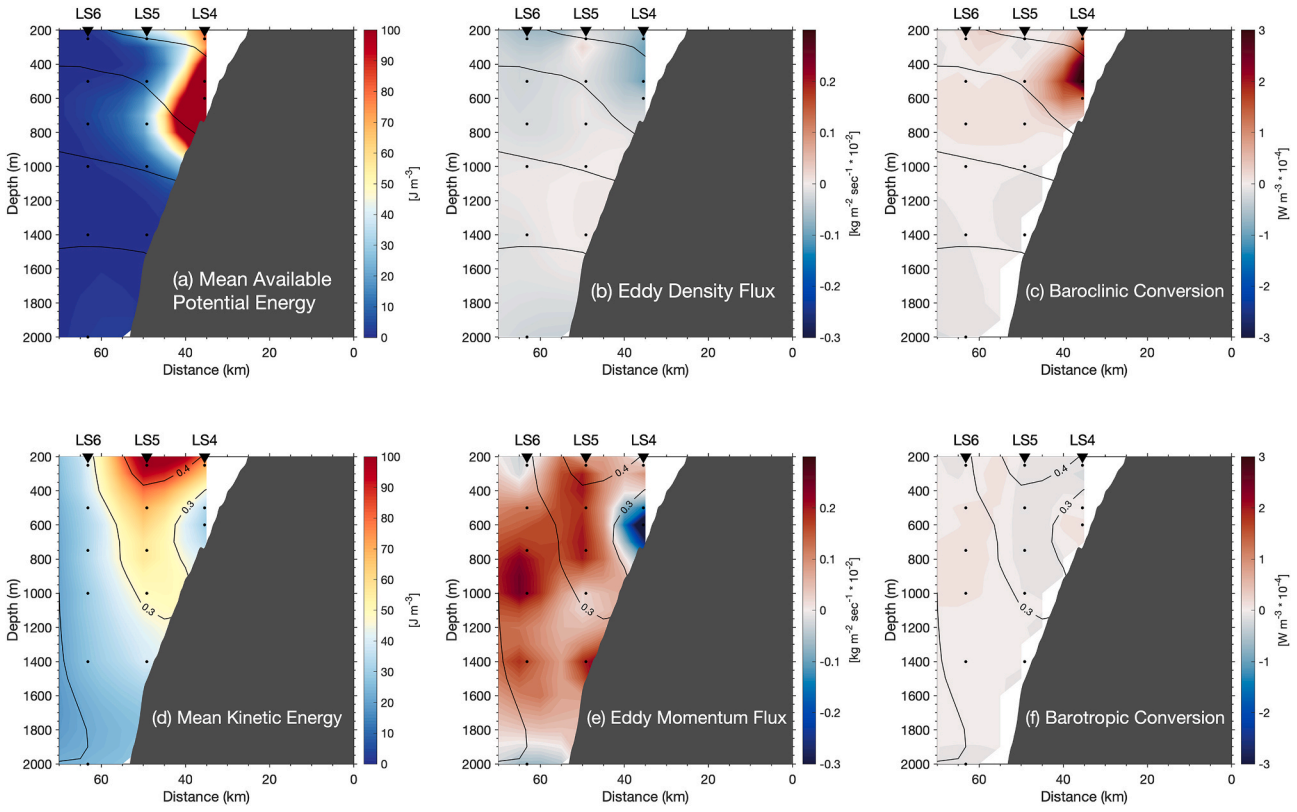

Fig. 10. Energetics components. (a) Mean available potential energy of the boundary current, (b) eddy density flux, and (c) baroclinic conversion rate. The mean isopycnals (kg m^{-3}) are contoured (a–c). (d) Mean kinetic energy of the boundary current, (e) eddy momentum flux, and (f) barotropic conversion rate. The mean along-stream flow (m s^{-1}) is contoured (d–f).

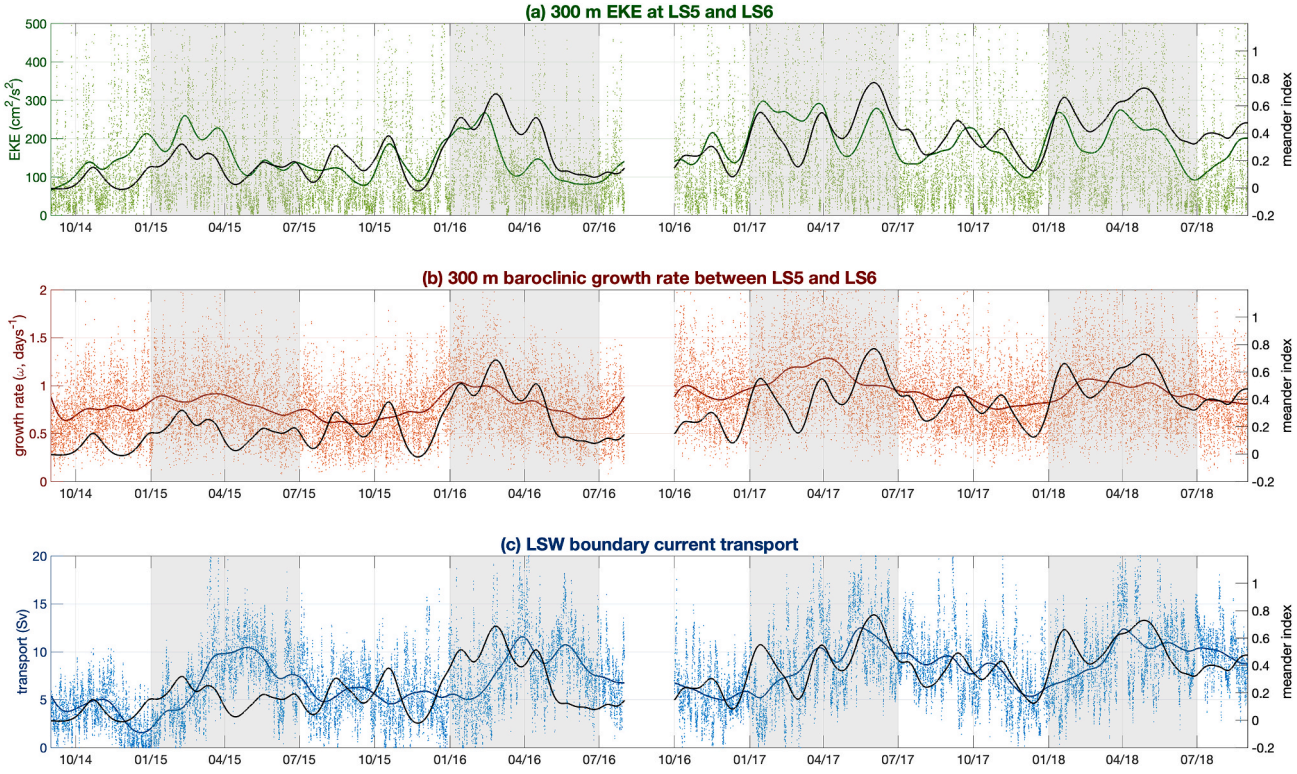

Fig. 11. (a) Timeseries of the meander index (defined in the text, black line in all three panels) compared against the EKE at 300 m averaged between moorings LS5 and LS6. (b) Timeseries of the meander index compared against baroclinic growth rate (see text for calculation details). (c) Timeseries of the meander index compared against LSW transport in the boundary current. In all three panels, the hourly data are plotted as points, and the 28-day lowpassed timeseries are plotted as solid curves.

Labrador Sea, and upstream in the Irminger Sea (e.g. Pickart et al., 2003b; le Bras et al., 2020). IW is the more highly stratified warm, saline, Atlantic-origin water mass advected around the subpolar gyre. While varying property definitions for LSW and IW exist (e.g. Clarke and Gascard, 1983; Krauss 1995; Lazier et al., 2002; Pickart et al., 2003a,b; Buch et al., 2004), for consistency we follow the definitions presented in Pacini et al. (2020) for LSW ($27.68\ kg/m^3 < \rho < 27.8\ kg/m^3$ and salinity < 34.92) and IW (salinity ≥ 34.92 and $\rho < 27.74\ kg/m^3$). Pacini et al. (2020) computed the volume transport of these two water masses and found that they are anti-correlated: when LSW transport is high (near the end of the winter convective season), IW transport is low, and, conversely, when LSW transport is low (in the fall), IW transport is high. This can be explained by two mechanisms: 1) the production of LSW and subsequent entrainment of this water into the boundary current as the convective season progresses, and 2) the direct cooling of IW through air-sea heat fluxes and through lateral mixing with LSW that alters the hydrographic properties of IW and converts it to LSW (Pacini et al., 2020). Notably, the seasonally-varying transport signals are dictated by the amount of each water mass in the boundary current, not the speed at which they travel.

We compare the LSW transport timeseries calculated by Pacini et al. (2020) to our meander index in Fig. 11c. One sees that when LSW transport is high – i.e. enhanced LSW presence and decreased IW presence in the boundary current – meander activity of the WGC is high (the correlation coefficient is 0.53, with $p < 0.01$). This provides a dynamical link between the seasonal production of LSW, the decreased stratification of the WGC, the enhanced baroclinic growth rate, and the development of boundary current meanders. This is consistent with previous model results (e.g. Spall, 2004).

3.3.3. What about 2015?

As noted in section 3.1, the winter/spring periods of 2016, 2017, and 2018 exhibited enhanced boundary current meandering, while this was not the case for 2015 (Fig. 3b). At the same time, the boundary current EKE was elevated all four years in winter/spring; however, the maximum in 2015 was less extensive than in the subsequent three years (Fig. 4). Furthermore, the seasonal increase in baroclinic growth rate was less pronounced in 2015 compared to the following three years (Fig. 11b).

A possible explanation for this lies in the recent trend in convective conditions in the Labrador and Irminger Seas. The period between 2012 and 2016 exhibited progressively deepening mixed layers and associated progressively denser newly-ventilated LSW production in the Labrador Sea, due to a persistent positive NAO phase and associated strong wintertime surface heat fluxes (Yashayaev and Loder, 2016). Additionally, convection was observed in the Irminger Sea and south of Cape Farewell beginning in winter 2015, with the deepest mixed layers observed in the 21st century in these regions (de Jong and de Steur, 2016; Fröb et al., 2016; Piron et al., 2017). Zunino et al. (2020) demonstrated that the period between 2015 and 2018 exhibited persistent deep convection south of Cape Farewell, due to strong air-sea buoyancy loss in 2015 and a preconditioned water column in the subsequent years.

This return to a regime of strong deep convection in the Labrador and Irminger Seas is consistent with the timeseries of LSW transport in the WGC, which displayed a linear increase of 1.21 Sv/yr over the four-year mooring measurement period (Fig. 12b, $R^2 = 0.41$; see also Section 3.5). We thus hypothesize that there was not enough weakly stratified LSW entering the WGC to destabilize the flow to the point of significant meander production in the winter of 2015, when LSW production was just beginning in the Irminger Sea and south of Cape Farewell and was still growing in the Labrador Sea. Recall that the presence of LSW in the boundary current affects the baroclinic growth rate in two ways, by influencing the stratification and by influencing the shear. Specifically, the more LSW that is present in the boundary current, the weaker the stratification is. At the same time, the more LSW is present offshore, the stronger the density gradient between the boundary current and the interior, and thus the stronger the shear is (via thermal wind). While in 2016, 2017, and 2018, the minimum in stratification is coincident with the maximum in shear, in 2015 these peaks are offset, such that the maximum in shear is achieved before the minimum in stratification, resulting in a weaker baroclinic growth rate. We note that if the timeseries of LSW transport is compared against the meander index for the first two years of data collection vs. the last two years, the correlation coefficient increases from 0.22 in 2015 and 2016 to 0.64 in 2017 and 2018 (compared to 0.53 when the four years are considered together).

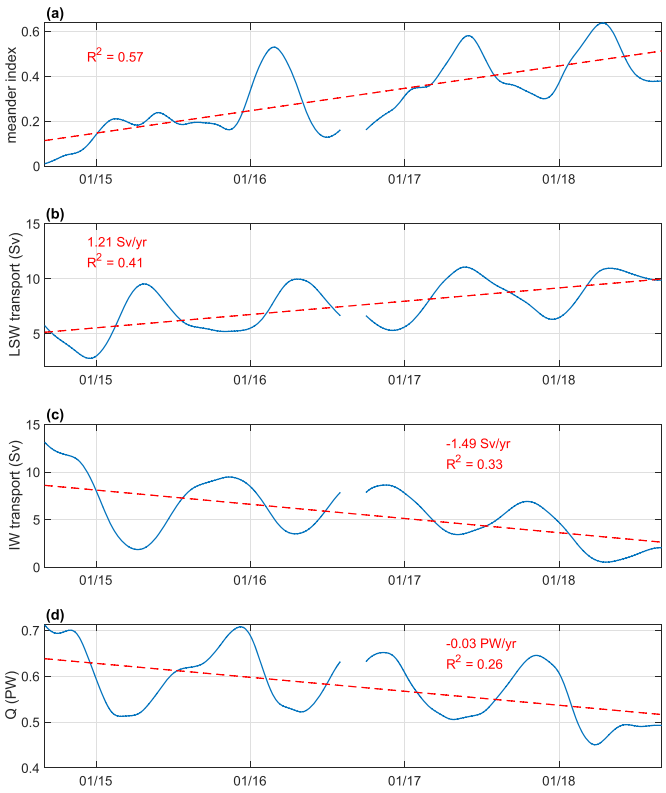

Fig. 12. Timeseries of 3-month lowpassed quantities. (a) meander index, (b) LSW transport, (c) IW transport, and (d) heat content of the boundary current. The linear fits are plotted as dashed red lines, and the yearly trends are indicated.

3.4. Implications for the interior Labrador Sea

Given the importance of the WGC to the stratification of the interior Labrador Sea (e.g. Chanut et al., 2008; Gelderloos et al., 2011; Rieck et al., 2019), we seek to estimate the possible contribution that the BCEs have to the heat content of the interior basin. The assumption is that some fraction of the meanders form oppositely signed pairs of eddies that then self-propagate into the interior (e.g. Spall et al., 2008), and that the anticyclone partner transports heat from the IW layer into the basin. The heat content of an individual eddy per unit area, relative to the temperature of interior LSW, ΔH_e, can be estimated following Hátún et al. (2007) and de Jong et al. (2014, 2016):

$$\Delta H_e = \rho_0 c_p \left(\overline{\theta_e} - \theta_{LSW}\right) D \left(\frac{r_e}{r_{LS}}\right)^2, \tag{9}$$

where

$$\theta_e = \frac{1}{\pi r_e^2} \int_0^{r_e} 2\pi r \theta(z, r) dr. \tag{10}$$

The quantity θ_e is the average temperature for a radially symmetric eddy, r_e is the radius of the eddy, ρ_0 is a reference density, c_p is the specific heat of water, r_{LS} is the radius of the convection region in the interior Labrador Sea, θ_{LSW} is the average temperature of 2016 LSW, and D is the depth of the eddy. Taking values of $\theta_e = 4.2$ °C (estimated from the composite feature, see Fig. 5a), $r_e = 10$ km (calculated above), $\rho_0 = 1027$ kg/m^3, $c_p = 4000$ J/(kg °C), $r_{LS} = 300$ km (Lilly et al., 2003), $\theta_{LSW} = 3.2$ °C (Yashayaev and Loder, 2017), and D = 1000 m, this yields a heat content of approximately 4.6 MJ/m^2 per BCE. This is roughly an order of magnitude less than the estimated heat content of a single IR (order 40 MJ/m^2; Hátún et al., 2007; de Jong et al., 2014; de Jong et al., 2016). As the boundary current circumnavigates the Labrador Sea, the temperature of the IW cools. Consequently, BCEs formed downstream of the OSNAP WG array will contain a smaller amount of heat. Assuming a linear decrease in temperature between the OSNAP array to the value presented in Pickart and Spall (2007) of 3.6 °C on the eastern side of the basin, we can account for this alongstream change in heat content.

Taking the length of the boundary current along which this process can occur to be 1500 km (d_{bc}), we then calculate how many features fit along the boundary current by computing $d_{bc}/(2*r_e)$ (75). This is repeated 50 times (due to an average rate of 50 features identified per year). Finally, we assume that 10% of these features evolve to form eddies, based on the fact that only 14/123 of the features identified at LS5 displayed negative alongstream flow at LS4 (implying that they were discrete anticyclonic eddies). This yields a total heat transfer 1.2 GJ/m^2 per year. This value compares favorably with the results of Straneo (2006), who computed an interior heat flux of 1 GJ/m^2 per year for a boundary current encircling a basin, meant to represent the Labrador Sea.

3.5. Trends

Past studies have addressed long-term trends in the hydrographic structure of the rim current system in the Labrador Sea. Myers et al. (2007) documented increasing temperature and salinity of the IW between 1995 and 2005. Similarly, in the FLAME model, de Jong et al. (2016) demonstrated an increasing density gradient between the interior Labrador Sea and the WGC due to a warming boundary current during a 15-year model run. In addition, Rykova et al. (2009) showed an increase in IR heat content using hydrographic data during the period 1990–2004.

Using the OSNAP WG mooring data, we now consider trends over the four-year period. As noted earlier, 2015 exhibited weak meandering compared to the subsequent years, possibly due to a regime shift in the prevalence of deep convection in 2015. This can be seen in Fig. 12a, where the meander index has been lowpassed using a 3-month filter (to highlight seasonality and long-term trends). The timeseries is well modeled with a linear fit, showing an increasing meander index over the four years of the record. Such an increase in meandering could help explain the trends observed in the model results of Rühs et al. (2021), where decreased convection is found in the northern and eastern Labrador Sea in recent years, coincident with a negative salinity trend (freshening) in the region. The idea is that more BCEs have been forming, transporting enhanced amounts of freshwater offshore within the surface layer of the eddies.

As previously described, meanders are triggered by baroclinic instability generated by the presence of LSW. Pacini et al. (2020) demonstrated that when transport of LSW is high seasonally, transport of IW is low and vice-versa. Here we see that as the transport of LSW increases linearly over the four years of data by 1.21 Sv/yr (Fig. 12b), the transport of IW decreases linearly by 1.47 Sv/yr (Fig. 12c). Since IW is the primary source of heat and salt to the boundary current, changes in the transport of IW can have implications for the heat content of the boundary current. We calculate the boundary current heat content according to

$$Q = \int_{z_w}^{z_e} \int_{-H}^{0} u\theta c_p \rho_0 dx dy \tag{11}$$

where u is the along-stream velocity at each grid point, θ is the associated temperature at each grid point, ρ_0 is the density, c_p is the heat capacity of sea water, H is the water column depth, and z_e and z_w are the eastern and western ends of the mooring array, respectively. The timeseries of heat content of the boundary current so calculated is shown in Fig. 12d and demonstrates that, concurrent with the long-term increase in LSW transport and decrease in IW transport, the heat content of the boundary current decreases by 0.03 PW/yr between 2015 and 2018. Hence, less heat can be fluxed to the interior to compensate for wintertime heat loss and production of LSW.

3.6. Downstream consequences

Previous work has shown that the EKE of the IR hotspot is enhanced in winter/spring (e.g. Brandt et al., 2004; de Jong et al., 2016), which is also the time of year when there is enhanced meandering of the WGC, as shown above. It is thus natural to wonder if the meanders are acting to trigger the formation of IRs.

To address this, we used the satellite altimetric data in conjunction with our mooring data. While the satellite-derived surface EKE clearly captures the IR hotspot signal (Fig. 13a, see also Brandt et al., 2004), it is unable to properly capture the variability of the WGC due to the small spatial scales of the meanders (there is only a weak surface EKE signature of the WGC in Fig. 13a). However, as seen in Fig. 13b, the satellite data do accurately depict the surface geostrophic velocity signal of the WGC. (North of the IR hotspot the boundary current signal weakens, which is also seen in the surface drifter data of Cuny et al. (2002). This could be due to a disruption of the flow by the IR formation mechanism).

Using the satellite data, the core of the surface WGC is defined as the grid point of maximum average surface velocity at each latitudinal cell (the red dots in Fig. 13b). We then constructed a latitude/time Hovmöller plot of WGC surface speed (Fig. 13c). While we are unable to construct an analogous Hovmöller plot for surface EKE, we can compare the timeseries of surface EKE at the IR hotspot with the mooring EKE at 300 m between LS5 and LS6 (Fig. 13d). In order to make the mooring EKE more comparable with the IR hotspot timeseries, we lowpassed the mooring data with a 7-day Butterworth filter (results are not sensitive to the exact choice of the filter width).

This highlights the coherence in seasonality of the two signals, with elevated values in winter and early spring. Care must be taken, however, to statistically quantify the relationship between the two timeseries. This is because, while the EKE product is daily, it is dependent on satellite pass density. However, the error estimates in the gridded product take this into account (Pujol et al., 2016). The daily average error of sea level height anomaly within the IR hotspot region (black box in Fig. 13a) is 5%. Propagating this into our EKE timeseries calculation gives the error bars shown in Fig. 13d (grey shading), indicating a large signal to noise ratio.

Fig. 14 shows the lagged correlation between the surface EKE at the IR hotspot and the mooring EKE at 300 m. This reveals two significant peaks: one at zero lag and the other at a lag of -15 days, where negative lags mean that the signal at the mooring array leads the signal at the IR hotspot. This indicates that there is both a simultaneous physical process at work and a propagating signal (note that these can't be distinguished in the Hovmöller plot). We suspect that the simultaneous process is due to offshore convection and LSW formation, which increases the lateral density gradient across the continental slope and therefore strengthens the WGC shear (through thermal wind). This would increase the instability everywhere along the current. The lagged signal could be due to the presence of LSW within the boundary current. In particular, when this water mass reaches a given site along the current, it alters the

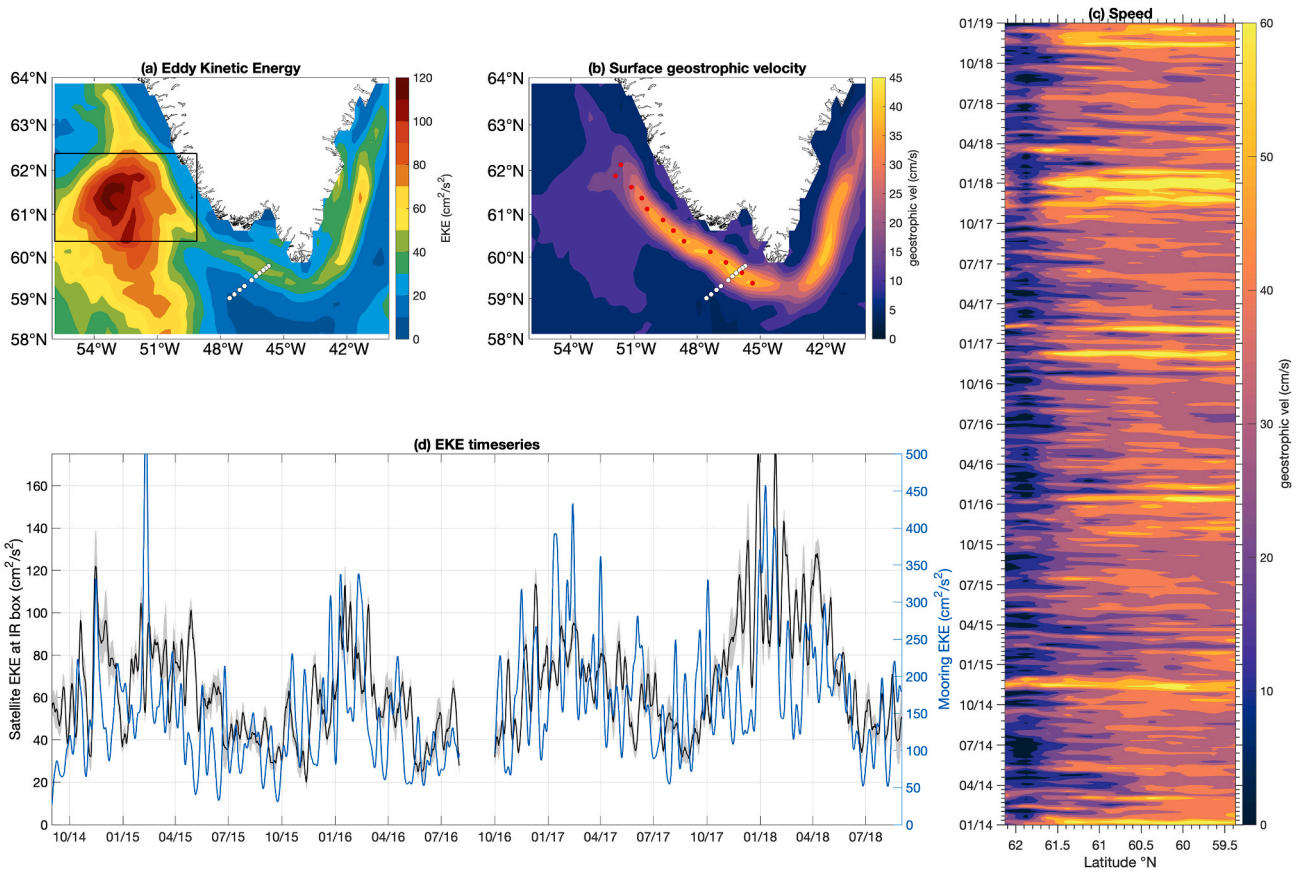

Fig. 13. (a) Map of the time-mean mean satellite-derived eddy kinetic energy, averaged between 2014 and 2018. The white dots indicate the OSNAP WG mooring array. (b) Same as (a) but for surface geostrophic velocity. The red dots indicate the core of the WGC, defined in the text. (c) Hövmoller diagram of geostrophic surface velocity along the WGC. (d) Comparison of satellite EKE at the IR box (defined in (a), black curve) with the mooring EKE in the WGC (blue curve). Grey shading on the black curve indicates the average error on the EKE measurement in the IR box, at each timestep.

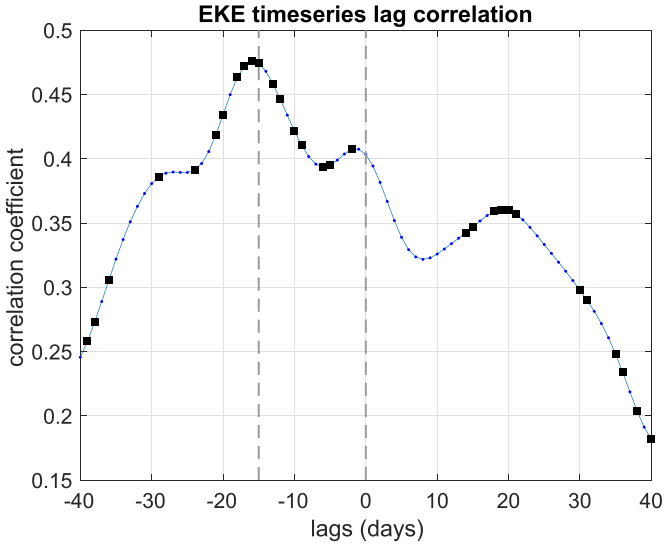

Fig. 14. Lagged correlations between the two EKE timeseries in Fig. 13d. The blue dots indicate the computed correlation at each lag, and the black squares indicate the statistically-significant values (based on the 95% confidence intervals calculated using the effective degrees of freedom).

stratification and thus leads to local instability. Notably, 15 days is the mean advective timescale for LSW to travel from the OSNAP WG site to the IR hotspot (at an advective speed of 30 cm s^{-1}, Pacini et al., 2020). Hence, as the water mass is advected by the current, it causes the instability to propagate with it. Our results thus suggest that enhanced meandering activity in the boundary current leads to enhanced formation of IRs. That said, more work is needed to investigate the dynamics by which this happens, including the role of the abrupt change in topographic slope at the formation location (e.g. Eden and Böning, 2002; Bracco and Pedlosky, 2003; Katsman et al., 2004).

4. Conclusions and discussion

Using four years of OSNAP mooring array data, abundant anticyclonic features and dipole pairs were observed at two moorings located in and seaward of the core of the mean WGC. The prevalence of these features was shown to be seasonal in nature, with increased activity during winter/spring of 2016, 2017, and 2018, consistent with enhanced boundary current EKE during these periods. The anticyclonic features diagnosed at the mooring within the core of the WGC exhibit decreased along-stream velocity, a reversal in cross-stream velocity, and bowling isopycnals from the surface to 1000 m. The features detected on the offshore edge of the WGC tended to occur in pairs—a leading anticyclonic feature and a trailing cyclonic feature. The anticyclonic portion of these features exhibited the same isopycnal and thermal structure as those at the core of the WGC, but instead exhibited enhanced along-stream velocity coincident with a reversal in cross-stream velocity. The features have an average wavelength of 20 km and account for 31% of the four-year mooring record.

Using kinematic evidence, together with potential vorticity considerations and satellite SST data, it was shown that the features are predominantly meanders of the WGC. This is consistent with the notion that the current can readily meander offshore, but is prohibited from meandering significantly onshore due to the steep bathymetry of the continental slope. It was argued that roughly 10% of the features corresponded to isolated vortices, suggesting that the meanders are able to grow to large enough amplitude to spawn eddies. These results constitute the first observational evidence for the existence of the BCEs that are commonly found in models of the Labrador Sea.

A stability analysis was performed revealing that baroclinic instability is responsible for the formation of the meanders. Furthermore, investigation of the stratification and shear of the boundary current demonstrated that the seasonal nature of the meandering can be explained by the decreased stratification in the boundary current due to increased LSW production and transport during winter/spring. The LSW contributes to a reduction in boundary current Ri and an increase in the baroclinic growth rate. It also helps to explain the lack of meandering observed in the first year of mooring observations (2015). During that time, LSW production was just starting to increase in the interior Labrador Sea as well as south of Cape Farewell and in the Irminger Sea. As such, the boundary current had not entrained enough LSW to destabilize it to the point of meander generation.

The importance of the meanders, and the associated BCEs that they form, for transferring heat into the interior basin was assessed by estimating the heat content of a given eddy. The average heat content of an individual feature at the mooring array was found to be 4.6 MJ/m^2. When summed over the length of the boundary current and the frequency of events, and taking into account the progressive cooling of the IW as it moves cyclonically around the basin, it was estimated that 1.2 GJ/m^2 of heat is transferred seasonally into the interior via BCEs. This is consistent with earlier high-resolution model results. It also implies that climate models must resolve these dynamics in order to accurately characterize LSW production and the lateral extent of the interior convective patch.

Finally, longer-term trends were investigated, revealing that the increased meandering over the four-year record is consistent with increased LSW presence in the boundary current. Simultaneously, increased LSW means decreased IW, which indicates decreased heat content of the boundary current, since IW has a higher heat content than LSW. This could result in two possible feedback loops, one positive and one negative. In the positive loop, increased convection results in increased LSW transport in the WGC, which in turn yields decreased heat transport in the boundary current, and thus restratification is less effective given the weaker heat fluxes associated with boundary current instabilities. In the negative loop, increased convection results in increased LSW transport in the WGC, which in turn yields increased BCE formation and thus increased heat flux from the boundary current to the interior. This would be more effective for restratification. Presently, it is unknown which of these scenarios dominates and if one might give way to the other; more data are required to track continued trends. In any event, models of the Labrador Sea must account for the changes in boundary current heat content by including LSW entrainment into the WGC and not relaxing boundary conditions back to a fixed value at Cape Farewell.

Data availability

All mooring data from the OSNAP WG array can be found at www.o-snap.org. The 2014–2016 mooring data are stored at https://doi.org/10.7924/r4fj2dr7k, and the 2016–2018 mooring data are stored at https://doi.org/10.35090/fz80-6c32. EU Copernicus Marine Service (CMEMS) sea surface height and geostrophic velocities are downloaded from https://resources.marine.copernicus.eu/?option=com_csw&task=results. Level 2 Modis 4 μm Aqua and Terra nighttime sea surface temperature (SST) data are downloaded from https://oceancolor.gsfc.nasa.gov/cgi/browse.pl?sen=amod.

Declaration of competing interest

The authors declare that they have no known competing financial interests or personal relationships that could have appeared to influence the work reported in this paper.

Acknowledgements

We thank John Kemp, Jim Ryder, Bryan Hogue, Andrew Davies, and Rick Trask for the design, fabrication and deployment of the mooring array. We thank the captain and crew of the RV Knorr and RV Neil Armstrong for the successful recovery and deployment of the OSNAP WG moorings in 2014, 2016, 2018, and 2020. We are grateful to three anonymous reviewers whose comments have strengthened the manuscript. A.P. and R.S.P. were funded by the National Science Foundation Grants OCE-1259618 and OCE-1756361.

References

Bracco, A., Pedlosky, J., 2003. Vortex generation by topography in locally unstable baroclinic flows. Journal of Physical Oceanography 33 (1), 207–219.

Brandt, P., Schott, F., Funk, A., Sena Martins, C., 2004. Seasonal to interannual variability of the eddy field in the Labrador Sea from satellite altimetry. J. Geophys. Res. 109, C02028 https://doi.org/10.1029/2002JC001551.

Brown, O.B., Minnett, P.J., 1999. MODIS Infrared Sea Surface Temperature Algorithm: Algorithm Theoretical Basis Document. Version 2.0. Available at. https://modis.gsfc.nasa.gov/data/atbd/atbd_mod25.pdf.

Bruce, G., 1995. Eddies southwest of the Denmark strait. Deep Sea Research 42 (I), 13–29.

Buch, E., Pedersen, S.A., Ribergaard, M.H., 2004. Ecosystem variability in west Greenland waters. Journal of Northwest Atlantic Fishery Science 34, 13–28. https://doi.org/10.2960/J.v34.m479.

Cessi, P., Wolfe, C.L., 2013. Adiabatic eastern boundary currents. Journal of Physical Oceanography 43 (6), 1127–1149. https://doi.org/10.1175/JPO-D-12-0211.1.

Chanut, J., Barńier, B., Large, W., Debreu, L., Penduff, T., Molines, J.M., Mathiot, P., 2008. Mesoscale eddies in the Labrador Sea and their contribution to convection and restratification. Journal of Physical Oceanography 38 (8), 1617–1643. https://doi.org/10.1175/2008JPO3485.1.

Cimoli, L., Stegner, A., Roullet, G., 2017. Meanders and eddy formation by a buoyant coastal current flowing over a sloping topography. Ocean Science 13 (6), 905–923. https://doi.org/10.5194/os-13-905-2017.

Clarke, R.A., Gascard, J.-C., 1983. The Formation of Labrador Sea water. Part I: large-scale processes. Journal of Physical Oceanography 13, 1764–1778. https://doi.org/10.1175/1520-0485(1983)013<1764:TFOLSW>2.0.CO, 2.

Colbourne, E.B., Narayanan, S., Prinsenberg, S., 1994. Climatic changes and environmental conditions in the Northwest Atlantic, 1970-1993. ICES Marine Science Symposia 198, 311–322.

Cuny, J., Rhines, P.B., Niiler, P.P., Bacon, S., 2002. Labrador Sea boundary currents and the fate of the Irminger Sea water. Journal of Physical Oceanography 32 (2), 627–647. https://doi.org/10.1175/1520-0485(2002)032<0627:LSBCAT>2.0.CO, 2.

de Jong, M.F., Bower, A.S., Furey, H.H., 2014. Two years of observations of warm-core anticyclones in the Labrador Sea and their seasonal cycle in heat and salt stratification. Journal of Physical Oceanography 44 (2), 427–444. https://doi.org/10.1175/JPO-D-13-070.1.

de Jong, M.F., Bower, A.S., Furey, H.H., 2016. Seasonal and interannual variations of Irminger ring formation and boundary-interior heat exchange in FLAME. Journal of Physical Oceanography 46 (6), 1717–1734. https://doi.org/10.1175/JPO-D-15-0124.1.

de Jong, M.F., de Steur, L., 2016. Strong winter cooling over the Irminger Sea in winter 2014–2015, exceptional deep convection, and the emergence of anomalously low SST. Geophysical Research Letters 43 (13), 7106–7113. https://doi.org/10.1002/2016GL069596.

Dickson, R., Brown, J., 1994. The production of North Atlantic deep water: sources, rates, and pathways. Journal of Geophysical Research 99 (C6), 12319–12341. https://doi.org/10.1029/94JC00530.

Eady, E.T., 1949. Long waves and cyclone waves. Tellus 1 (3), 33–52. https://doi.org/10.3402/tellusa.v1i3.8507.

Eden, C., Böning, C., 2002. Sources of eddy kinetic energy in the Labrador Sea. Journal of Physical Oceanography 32 (12), 3346–3363. https://doi.org/10.1175/1520-0485(2002)032<3346:SOEKEI>2.0.CO, 2.

Elipot, S., Beal, L.M., 2015. Characteristics, energetics, and origins of agulhas current meanders and their limited influence on ring shedding. Journal of Physical Oceanography 45 (9), 2294–2314. https://doi.org/10.1175/JPO-D-14-0254.1.

Fischer, J., Visbeck, M., Zantopp, R., Nunes, N., 2010. Interannual to decadal variability of outflow from the Labrador Sea. Geophysical Research Letters 37 (24), 1–5. https://doi.org/10.1029/2010GL045321.

Florindo-López, C., Bacon, S., Aksenov, Y., Chafik, L., Colbourne, E., Penny Holliday, N., 2020. Arctic Ocean and Hudson Bay freshwater exports: new estimates from seven decades of hydrographic surveys on the Labrador Shelf. Journal of Climate 33 (20), 8849–8868. https://doi.org/10.1175/JCLI-D-19-0083.1.

Fröb, F., Olsen, A., Vage, K., Moore, G.W., Yashayaev, I., Jeansson, E., Rajasakaren, B., 2016. Irminger Sea deep convection injects oxygen and anthropogenic carbon to the ocean interior. Nature Communications 7. https://doi.org/10.1038/ncomms13244.

Gascard, J.-C., Clarke, R.A., 1983. The Formation of Labrador Sea water. Part II: mesoscale and smaller-scale processes. Journal of Physical Oceanography 13, 1779–1797.

Gelderloos, R., Katsman, C.A., Drijfhout, S.S., 2011. Assessing the roles of three eddy types in restratifying the Labrador Sea after deep convection. Journal of Physical Oceanography 41 (11), 2102–2119. https://doi.org/10.1175/JPO-D-11-054.1.

Lab Sea Group, 1998. The Labrador Sea Deep Convection Experiment. Bulletin of the American Meteorological Society 79 (10), 2033–2058. https://doi.org/10.1175/1520-0477(1998)079<2033:tlsdce>2.0.co;2.

Hátún, H., Eriksen, C.C., Rhines, P.B., 2007. Buoyant eddies entering the Labrador Sea observed with gliders and altimetry. Journal of Physical Oceanography 37 (12), 2838–2854. https://doi.org/10.1175/2007JPO3567.1.

Havik, L., Vage, K., Pickart, R.S., Harden, B., Von Appen, W.J., Jonsson, S., Osterhus, S., 2017. Structure and variability of the shelfbreak East Greenland current north of Denmark strait. Journal of Physical Oceanography 47 (10), 2631–2646. https://doi.org/10.1175/JPO-D-17-0062.1.

Huang, J., Pickart, R.S., Valdimarsson, H., Lin, P., Spall, M.A., Xu, F., 2019. Structure and variability of the north Icelandic jet from Two years of mooring data. Journal of Geophysical Research: Oceans 124 (6), 3987–4002. https://doi.org/10.1029/2019JC015134.

Hurrell, J., 1995. Decadal trends in the North Atlantic oscillation: regional temperatures and precipitation. Science 269, 676–697. https://doi.org/10.1126/science.269.5224.676.

Jones, H., Marshall, J., 1997. Restratification after deep convection. Journal of Physical Oceanography 27 (10), 2276–2287. https://doi.org/10.1175/1520-0485(1997)027<2276:RADC>2.0.CO;2.

Katsman, C.A., Spall, M.A., Pickart, R.S., 2004. Boundary current eddies and their role in the restratification of the Labrador Sea. Journal of Physical Oceanography 34 (9), 1967–1983. https://doi.org/10.1175/1520-0485(2004)034<1967:BCEATR>2.0.CO, 2.

Khatiwala, S., Tanhua, T., Mikaloff Fletcher, S., Gerber, M., Doney, S.C., Graven, H.D., Gruber, N., McKinley, G.A., Murata, A., Ríos, A.F., Sabine, C.L., 2013. Global ocean storage of anthropogenic carbon. Biogeosciences 10 (4), 2169–2191. https://doi.org/10.5194/bg-10-2169-2013.

Krauss, W., 1995. Currents and mixing in the Irminger Sea and in the Iceland basin. Journal of Geophyisical Research 100, 10851–10871. https://doi.org/10.1029/95JC00423.

Lazier, J.R.N., Wright, D.G., 1993. Annual velocity variations in the Labrador current. Journal of Physical Oceanography 23, 659–678. https://doi.org/10.1175/1520-0485(1993)023, 0659:AVVITL.2.0.CO;2.

Lazier, J., Hendry, R., Clarke, A., Yashayaev, I., Rhines, P., 2002. Convection and restratification in the Labrador Sea, 1990-2000. Deep-Sea Research Part I: Oceanographic Research Papers 49 (10), 1819–1835. https://doi.org/10.1016/S0967-0637(02)00064-X.

Le Bras, I.A., Straneo, F., Holte, J., de Jong, M.F., Holliday, N.P., 2020. Rapid export of waters formed by convection near the Irminger Sea's western boundary. Geophysical Research Letters 47, 1–10. https://doi.org/10.1029/2019GL085989.

Li, F., Susan Lozier, M., Danabasoglu, G., Holliday, N.P., Kwon, Y.O., Romanou, A., Yeager, S.G., Zhang, R., 2019. Local and downstream relationships between Labrador Sea water volume and North Atlantic meridional overturning circulation variability. Journal of Climate 32 (13), 3883–3898. https://doi.org/10.1175/JCLI-D-18-0735.1.

Lilly, J.M., Rhines, P.B., 2002. Coherent eddies in the Labrador Sea observed from a mooring. Journal of Physical Oceanography 32 (2), 585–598. https://doi.org/10.1175/1520-0485(2002)032<0585:CEITLS>2.0.CO, 2.

Lilly, J.M., Rhines, P.B., Schott, F., Lavender, K., Lazier, J., Send, U., Asaro, E.D., 2003. Observations of the Labrador Sea eddy field. Progress in Oceanography 59, 75–176. https://doi.org/10.1016/j.pocean.2003.08.013.

Lilly, J.M., Rhines, P.B., Visbeck, M., Davis, R., Lazier, J.R., Schott, F., Farmer, D., 1999. Observing deep convection in the Labrador Sea during winter 1994/95. Journal of Physical Oceanography 29 (8 PART 2), 2065–2098. https://doi.org/10.1175/1520-0485(1999)029<2065:odcitl>2.0.co, 2.

Lin, P., Pickart, R.S., Torres, D.J., Pacini, A., 2018. Evolution of the freshwater coastal current at the Southern Tip of Greenland. Journal of Physical Oceanography 48 (9), 2127–2140. https://doi.org/10.1175/JPO-D-18-0035.1.

Lozier, M.S., Bacon, S., Bower, A.S., Cunningham, S.A., de Jong, M.F., de Steur, L., de Young, B., Fischer, J., Gary, S.F., Greenan, B.J., Heimbmbach, P., Holliday, N.P., Houpert, L., Inall, M.E., Johns, W.E., Johnson, H.L., Karstensen, J., Li, F., Lin, X., Mackay, N., Marshall, D.P., Mercier, H., Myers, P.G., Pickart, R.S., Pillar, H.R., Straneo, F., Thierry, V., Weller, R.A., Williams, R.G., Wilson, C., Yang, J., Zhao, J., Zika, J.D., 2017. Overturning in the Subpolar North Atlantic Program: a new international ocean observing system. Bulletin of the American Meteorological Society 98 (4), 737–752. https://doi.org/10.1175/BAMS-D-16-0057.1.

Lozier, M.S., Li, F., Bacon, S., Bahr, F., Bower, A.S., Cunningham, S.A., de Jong, M.F., de Steur, L., DeYoung, B., Fischer, J., Gary, S.F., Greenan, B.J., Holliday, N.P., Houk, A., Houpert, L., Inall, M.E., Johns, W.E., Johnson, H.L., Johnson, C., Karstensen, J., Koman, G., Le Bras, I.A., Lin, X., Mackay, N., Marshall, D.P., Mercier, H., Oltmanns, M., Pickart, R.S., Ramsey, A.L., Rayner, D., Straneo, F., Thierry, V., Torres, D.J., Williams, R.G., Wilson, C., Yang, J., Yashayaev, I., Zhao, J., 2019. A sea change in our view of overturning in the subpolar North Atlantic. Science 363 (6426), 516–521. https://doi.org/10.1126/science.aau6592.

Myers, P.G., Kulan, N., Ribergaard, M.H., 2007. Irminger water variability in the west Greenland current. Geophysical Research Letters 34 (17), 2–7. https://doi.org/10.1029/2007GL030419.

Pacini, A., Pickart, R.S., Bahr, F., Torres, D.J., Ramsey, A.L., Holte, J., Karstensen, J., Oltmanns, M., Straneo, F., Le Bras, I.A., Moore, G.W., Femke de Jong, M., 2020. Mean conditions and seasonality of the west Greenland boundary current system near cape farewell. Journal of Physical Oceanography 50 (10), 2849–2871. https://doi.org/10.1175/JPO-D-20-0086.1.

Pacini, A., Pickart, R.S., Le Bras, I.A., Straneo, F., Holliday, N., Spall, M., 2021. Cyclonic eddies in the west Greenland boundary current system. Journal of Physical Oceanography 1–45. https://doi.org/10.1175/jpo-d-20-0255.1.

Pawlowicz, R., Beardsley, B., Lentz, S., 2002. Classical tidal harmonic analysis including error estimates in MATLAB using TDE. Computers and Geosciences 28 (8), 929–937. https://doi.org/10.1016/S0098-3004(02)00013-4.

Penduff, T., Barnier, B., Dewar, W.K., O'Brien, J.J., 2004. Dynamical response of the oceanic eddy field to the North Atlantic Oscillation: a model-data comparison. Journal of Physical Oceanography 34 (12), 2615–2629. https://doi.org/10.1175/JPO2618.1.

Pennelly, C., Myers, P.G., 2020. Introducing LAB60: a 1/60 ° NEMO 3.6 numerical simulation of the Labrador Sea. Geoscientific Model Development 13 (10), 4959–4975. https://doi.org/10.5194/gmd-13-4959-2020.

Pickart, R.S., 1992. Water mass components of the North Atlantic deep western boundary current. Deep Sea Res. Part I: Oceanogr. Res. P. 39 (9), 1553–1572. https://doi.org/10.1016/0198-0149(92)90047-W.

Pickart, R.S., Spall, M.A., 2007. Impact of Labrador Sea convection on the north Atlantic meridional overturning circulation. Journal of Physical Oceanography 37 (9), 2207–2227. https://doi.org/10.1175/JPO3178.1.

Pickart, R.S., Spall, M.A., Ribergaard, M.H., Moore, G.W., Milliff, R.F., 2003b. Deep convection in the Irminger Sea forced by the Greenland tip jet. Nature 424 (6945), 152–156. https://doi.org/10.1038/nature01729.

Pickart, R.S., Straneo, F., Moore, G.W.K., 2003a. Is Labrador Sea water formed in the Irminger basin? Deep Sea Research I 50, 23–52. https://doi.org/10.1016/S0967-0637(02)00134-6.

Pickart, R.S., Torres, D.J., Clarke, R.A., 2002. Hydrography of the Labrador Sea during active convection. Journal of Physical Oceanography 32 (2), 428–457. https://doi.org/10.1175/1520-0485(2002)032<0428:HOTLSD>2.0.CO, 2.

Pickart, R.S., Torres, D.J., Fratantoni, P.S., 2005. The East Greenland spill jet. Journal of Physical Oceanography 35 (6), 1037–1053. https://doi.org/10.1175/JPO2734.1.

Piron, A., Thierry, V., Mercier, H., Caniaux, G., 2017. Gyre-scale deep convection in the subpolar North Atlantic Ocean during winter 2014–2015. Geophysical Research Letters 44 (3), 1439–1447. https://doi.org/10.1002/2016GL071895.

Prater, M.D., 2002. Eddies in the Labrador Sea as observed by profiling RAFOS floats and remote sensing. Journal of Physical Oceanography 32 (2), 411–427. https://doi.org/10.1175/1520-0485(2002)032<0411:EITLSA>2.0.CO, 2.

Pujol, M.I., Faugère, Taburet, G., Dupuy, S., Pelloquin, M.A., Picot, N., 2016. DUACS DT2014: the new multi-mission altimeter data set reprocessed over 20 years. Ocean Science 12, 1067–1090. https://doi.org/10.5194/os-12-1067-2016.

Rhein, M., Fischer, J., Smethie, W.M., Smythe-Wright, D., Weiss, R.F., Mertens, C., Min, D.H., Fleischmann, U., Putzka, A., 2002. Labrador Sea water: pathways, CFC inventory, and formation rates. Journal of Physical Oceanography 32 (2), 648–665. https://doi.org/10.1175/1520-0485(2002)032<0648:LSWPCI>2.0.CO, 2.

Rieck, J.K., Böning, C.W., Getzlaff, K., 2019. The nature of eddy kinetic energy in the labrador sea: different types of mesoscale eddies, their temporal variability, and impact on deep convection. Journal of Physical Oceanography 49 (8), 2075–2094. https://doi.org/10.1175/JPO-D-18-0243.1.

Rieck, J.K., Böning, C.W., Greatbatch, R.J., Scheinert, M., 2015. Seasonal variability of eddy kinetic energy in a global high-resolution ocean model. Geophysical Research Letters 42 (21), 9379–9386. https://doi.org/10.1002/2015GL066152.

Rühs, S., Oliver, A.C.J., Biastoch, A., Böning, C.W., Dowd, M., Getzlaff, K., Martin, T., Myers, P.G., 2021. Changing spatial patterns of deep convection in the subpolar North Atlantic. Journal of Geophysical Research: Oceans 126, e2021JC017245. https://doi.org/10.1029/2021JC017245.

Rykova, T., Straneo, F., Bower, A.S., 2015. Seasonal and interannual variability of the west Greenland current system in the Labrador Sea in 1993-2008. Journal of Geophysical Research: Oceans 120, 1318–1332. https://doi.org/10.1002/2014JC010386.

Rykova, T., Straneo, F., Lilly, J.M., Yashayaev, I., 2009. Irminger current anticyclones in the Labrador Sea observed in the hydrographic record, 1990-2004. Journal of Marine Research 67 (3), 361–384. https://doi.org/10.1357/002224009789954739.

Send, U., Marshall, J., 1995. Integral effects of deep convection. Journal of Physical Oceanography 25, 855–872. https://doi.org/10.1175/1520-0485(1995)025.<0855:IEODC>2.0.CO;2.

Smith, W.H.F., Wessel, P., 1990. Gridding with continuous curvature splines in tension. Geophysics 55 (3), 293–305. https://doi.org/10.1190/1.1442837.

Spall, M.A., 2004. Boundary currents and watermass transformation in marginal seas. Journal of Physical Oceanography 34 (5), 1197–1213. https://doi.org/10.1175/1520-0485(2004)034<1197:BCAWTI>2.0.CO, 2.

Spall, M.A., 2010. Dynamics of down welling in an eddy-resolving convective basin. Journal of Physical Oceanography 40 (10), 2341–2347. https://doi.org/10.1175/2010JPO4465.1.

Spall, M.A., Pedlosky, J., 2008. Lateral coupling in baroclinically unstable flows. Journal of Physical Oceanography 38 (6), 1267–1277. https://doi.org/10.1175/2007JPO3906.1.

Spall, M.A., Pickart, R.S., 2001. Where does dense water sink? a subpolar gyre example. Journal of Physical Oceanography 31 (3), 810–826. https://doi.org/10.1175/1520-0485(2001)031<0810:WDDWSA>2.0.CO, 2.

Spall, M.A., Pickart, R.S., Fratantoni, P.S., Plueddemann, A.J., 2008. Western Arctic shelfbreak eddies: formation and Transport. Journal of Physical Oceanography 38 (8), 1644–1668. https://doi.org/10.1175/2007JPO3829.1.

Spall, M.A., Price, J.F., 1998. Mesoscale variability in Denmark strait: The PV outflow hypothesis. Journal of Physical Oceanography 28, 1598–1623.

Stone, P.H., 1970. On non-geostrophic baroclinic stability: Part II. Journal of the Atmospheric Sciences 27, 721–726.

Straneo, F., 2006. Heat and freshwater transport through the central Labrador Sea. Journal of Physical Oceanography 36 (4), 606–628. https://doi.org/10.1175/JPO2875.1.

Sutherland, D.A., Straneo, F., Stenson, G.B., Davidson, F.J., Hammill, M.O., Rosing-Asvid, A., 2013. Atlantic water variability on the SE Greenland continental shelf and its relationship to SST and bathymetry. Journal of Geophysical Research: Oceans 118 (2), 847–855. https://doi.org/10.1029/2012JC008354.

Sy, A., Rheint, M., Lazier, J.R., Koltermann, K.P., Meincke, J., Putzka, A., Bersch, M., 1997. Surprisingly rapid spreading of newly formed intermediate waters across the North Atlantic Ocean. Nature 386 (6626), 675–679. https://doi.org/10.1038/386675a0.

Tagklis, F., Bracco, A., Ito, T., Castelao, R.M., 2020. Submesoscale modulation of deep water formation in the Labrador Sea. Scientific Reports 10 (1), 1–13. https://doi.org/10.1038/s41598-020-74345-w.

Takahashi, T., Coauthors, 2009. Climatological mean and de- cadal change in surface ocean pCO2, and net sea-air CO2 flux over the global oceans. Deep Sea Research II 56, 554–577. https://doi.org/10.1016/j.dsr2.2008.12.009.

Talley, L., McCartney, M., 1982. Distribution and circulation of Labrador Sea water. Journal of Physical Oceanography 12, 1189–1205.

Thomsen, S., Carsten, E., Czeschel, L., 2014. Stability analysis of the Labrador current. Journal of Physical Oceanography 44 (2), 445–463. https://doi.org/10.1175/JPO-D-13-0121.1.

Vage, K., Pickart, R.S., Thierry, V., Reverdin, G., Lee, C.M., Petrie, B., Agnew, T.A., Wong, A., Ribergaard, M.H., 2009. Surprising return of deep convection to the subpolar North Atlantic Ocean in winter 2007-2008. Nature Geoscience 2 (1), 67–72. https://doi.org/10.1038/ngeo382.

Vallis, G.K., 2006. Atmospheric and Oceanic Fluid Dynamics: Fundamentals and Large-Scale Circulation. Cambridge University Press.

von Appen, W.J., Pickart, R.S., 2012. Two configurations of the western Arctic shelfbreak current in summer. Journal of Physical Oceanography 42, 329–351. https://doi.org/10.1175/JPO-D-11-026.1.

von Appen, W.J., Pickart, R.S., Brink, K.H., Haine, T.W., 2014. Water column structure and statistics of Denmark Strait Overflow Water cyclones. Deep- Sea Research Part I: Oceanographic Research Papers 84, 110–126. https://doi.org/10.1016/j.dsr.2013.10.007.

von Appen, W.J., Schauer, U., Hattermann, T., Beszczynska-Möller, A., 2016. Seasonal cycle of mesoscale instability of the west spitsbergen current. Journal of Physical Oceanography 46 (4), 1231–1254. https://doi.org/10.1175/JPO-D-15-0184.1.

Yashayaev, I., Loder, J.W., 2016. Recurrent replenishment of Labrador Sea Water and associated decadal-scale variability. Journal of Geophysical Research: Oceans 121 (8), 8095–8114.

Yashayaev, I., Loder, J.W., 2017. Further intensification of deep convection in the Labrador Sea in 2016. Geophysical Research Letters 44 (3), 1429–1438.

Zou, et al., 2021. Observed deep cyclonic eddies around southern Greenland. Journal of Physical Oceanography 51 (10), 3235–3252. https://doi.org/10.1175/JPO-D-20-0288.1.

Zunino, P., Mercier, H., Thierry, V., 2020. Why did deep convection persist over four consecutive winters (2015-2018) southeast of Cape Farewell? Ocean Science 16 (1), 99–113. https://doi.org/10.5194/os-16-99-2020.